

# Supplementary Material for: Hyperbolic Non-Abelian Semimetal

Tarun Tummuru ,<sup>1</sup> Anffany Chen ,<sup>2</sup> Patrick M. Lenggenhager ,<sup>1,3,4,5</sup>  
Titus Neupert ,<sup>1</sup> Joseph Maciejko ,<sup>2,6</sup> and Tomáš Bzdušek ,<sup>1,3</sup>

<sup>1</sup>*Department of Physics, University of Zurich, Winterthurerstrasse 190, 8057 Zurich, Switzerland*

<sup>2</sup>*Department of Physics & Theoretical Physics Institute,  
University of Alberta, Edmonton, Alberta T6G 2E1, Canada*

<sup>3</sup>*Condensed Matter Theory Group, Paul Scherrer Institute, 5232 Villigen PSI, Switzerland*

<sup>4</sup>*Institute for Theoretical Physics, ETH Zurich, 8093 Zurich, Switzerland*

<sup>5</sup>*Max Planck Institute for the Physics of Complex Systems, Nöthnitzer Str. 38, 01187 Dresden, Germany*

<sup>6</sup>*Quantum Horizons Alberta, University of Alberta, Edmonton, Alberta T6G 2E1, Canada*

## CONTENTS

I. PBC clusters	1
A. Large-index normal subgroups from intersection	1
B. Adjacency matrix	3
C. Hamiltonian construction	3
D. Flux insertion	4
II. U( $d$ )-HBT	4
III. Supercell method	5
A. Hyperbolic translation groups	5
B. Hyperbolic Brillouin zones	5
C. 2-supercell approximation	6
1. Abelian Bloch Hamiltonian for 2-supercells	7
2. Mass dependence of the nodal manifold	8
3. Symmetry protection of the nodal ring	9
D. Density of states for larger $n$ -supercells	11
1. Density of states from random sampling	11
2. Fitting the low-energy density of states	13
3. Metal-to-insulator transition for large $n$ -supercells	16
References	16

## I. PBC CLUSTERS

PBC clusters are finite-sized hyperbolic lattices with periodic boundary conditions (PBC). Owing to the spatial curvature, applying PBC to a finite  $\{p, q\}$  hyperbolic lattice is a nontrivial task relying on geometric group theory [1–4]. In this section, we describe our method for constructing PBC clusters, which applies to  $\{p, q\}$  lattices with known hyperbolic Bravais lattices and corresponding unit cells [5–7]. The hyperbolic translation group  $\Gamma$  of a hyperbolic Bravais lattice is generated by elements  $\gamma_j$  which relate pairs of edges of the primitive cell. A PBC cluster with  $N$  primitive cells is defined by a choice of normal subgroup  $\tilde{\Gamma} \triangleleft \Gamma$  of index  $N$  corresponding to a set of translations under which the wave function is invariant [2]. Given such a normal subgroup, one can compute the factor group  $\Gamma/\tilde{\Gamma}$ , which is a finite group of order  $N$  and corresponds to a group of translations modulo PBC on the finite cluster. The structure of the factor group allows us to construct an adjacency matrix

A on the cluster, in which each lattice site corresponds to a coset  $[\eta] \in \Gamma/\tilde{\Gamma}$ . We use  $[\eta]$  to denote the right coset of  $\eta \in \Gamma$ , i.e.,  $[\eta] = \tilde{\Gamma}\eta = \{\tilde{\eta}\eta : \tilde{\eta} \in \tilde{\Gamma}\}$ . More complicated tight-binding models—with multiple on-site degrees of freedom (e.g., orbitals or sublattices)—can then be built by tensoring the adjacency matrix  $A$  with finite-dimensional matrices in orbital/sublattice space. PBC clusters with Abelian factor group  $\Gamma/\tilde{\Gamma}$  are termed Abelian clusters, and such clusters exclude all higher-dimensional IRs of the translation group. To study the gapless spectrum of the hyperbolic non-Abelian semimetal, we focus on non-Abelian clusters, whose factor group is non-Abelian and allows us to discretely sample the spectrum of non-Abelian Bloch states.

In the following, we outline our methodology for constructing the tight-binding Dirac model on *arbitrarily large* non-Abelian PBC clusters of the  $\{8, 8\}$  hyperbolic (Bravais) lattice, with hyperbolic translation group  $\Gamma$  defined in Eq. (2). Section IA presents a method based on subgroup intersection to overcome the computational limitations of Ref. [2], in which only modest system sizes  $N \leq 25$  had been reached. The algorithm to construct the adjacency matrix  $A$  on a PBC cluster is explained in Section IB. Finally, in Section IC, we construct the Hamiltonian for the hyperbolized QHI model.

### A. Large-index normal subgroups from intersection

In Ref. [2], a GAP implementation [8, 9] of the low-index normal subgroups procedure [10] was used to enumerate all normal subgroups  $\tilde{\Gamma}$  up to a given finite index  $N_{\max}$ . Such a procedure is computationally expensive, and Ref. [2] only presented results for PBC clusters of maximum size  $N_{\max} = 25$ . To overcome these limitations, we propose an algorithm based on a few mathematical results. First, given two normal subgroups  $\tilde{\Gamma}^{(1)}, \tilde{\Gamma}^{(2)}$  of the Fuchsian translation group  $\Gamma$ , we show that their intersection  $\tilde{\Gamma}^{(1)} \cap \tilde{\Gamma}^{(2)}$  is also normal in  $\Gamma$  and thus defines a valid PBC cluster. In the following, we denote set inclusion by  $\subseteq$ , subgroup inclusion by  $\leq$ , and normal subgroup inclusion by  $\triangleleft$ .

**Lemma I.1.** *Let  $H, K \triangleleft G$ . Then  $H \cap K \triangleleft G$ .*

*Proof.* First, we prove that  $H \cap K \leq G$ . If  $g, h \in H \cap K$ , they are also in  $H$ . Since  $H$  is a group, then  $gh \in H$ . On the other hand,  $g, h$  are also in  $K$ , and since  $K$  is also a group, we have

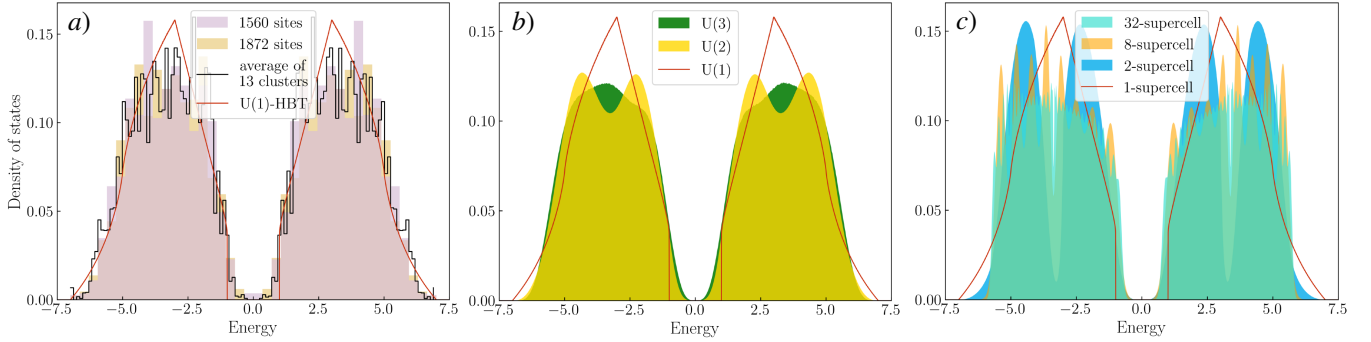


FIG. S1. A comparison of different techniques to access non-Abelian Bloch states in the hyperbolic QHI model at  $m = 3$ . (a) Sample DOS of two PBC clusters, alongside the average of 13 clusters (120 bins), per the discussion in Sec. I. (b)  $U(d)$ -HBT for  $d = 1, 2$  and 3, as described in Sec. II. While  $U(1)$ -HBT is gapped, spectra of higher-dimensional IRs are semimetallic. (c) Modelling with the supercell approach discussed in Sec. III. Going beyond the 2-supercell, we observe a gradual convergence to a smooth DOS curve in the limit of large supercells. The converged DOS curve appears to be insulating at  $m = 3$ , see Sec. III D.

$gh \in K$ . Since  $gh$  is both in  $H$  and in  $K$ , we have  $gh \in H \cap K$ . But this holds for every pair of elements  $g, h$  in  $H \cap K$ , thus  $H \cap K$  is a group. Since  $H \cap K$  is contained in  $G$  as a set, it is a subgroup of  $G$ .

Next, we prove that  $H \cap K$  is normal in  $G$ . Consider an element  $b$  of the set  $g(H \cap K)$ . Since  $H$  contains  $H \cap K$ , it is also true that  $b \in gH$ , and since  $K$  also contains  $H \cap K$ , it is also true that  $b \in gK$ . Therefore,  $b$  must belong to the intersection  $gH \cap gK$ . Since this is true for any  $b \in g(H \cap K)$ , we have  $g(H \cap K) \subseteq gH \cap gK$ . However, we can also show that the converse is true:  $gH \cap gK \subseteq g(H \cap K)$ . Let  $b \in gH \cap gK$ . Then,  $b \in gH$  and  $b \in gK$ , and there exist  $h \in H$  and  $k \in K$  such that  $b = gh = gk$ . Multiplying by  $g^{-1}$ , we find that  $h = k \in H \cap K$ . Thus,  $b \in g(H \cap K)$ , and since  $b$  was otherwise arbitrary, we find that  $gH \cap gK \subseteq g(H \cap K)$ . Since both  $g(H \cap K) \subseteq gH \cap gK$  and  $gH \cap gK \subseteq g(H \cap K)$  are true, we necessarily have that  $g(H \cap K) = gH \cap gK$ . We leave it as an exercise to the reader to also prove using exactly the same arguments that  $(H \cap K)g = Hg \cap Kg$ .

We finally show that the latter two equalities imply normality of  $H \cap K$  in  $G$ . Let  $g \in G$ , then  $H \triangleleft G$  implies  $gH = Hg$ , and  $K \triangleleft G$  implies  $gK = Kg$ . Therefore,  $g(H \cap K) = gH \cap gK = Hg \cap Kg = (H \cap K)g$ , thus  $H \cap K \triangleleft G$ .  $\square$

Next, we show that the index of  $\tilde{\Gamma}^{(1)} \cap \tilde{\Gamma}^{(2)}$  is bounded from below by the least common multiple of the indices of  $\tilde{\Gamma}^{(1)}$  and  $\tilde{\Gamma}^{(2)}$ , and is thus typically larger than either individual index.

**Lemma I.2.** *Let  $H, K \triangleleft G$  with indices  $|G : H| = m$  and  $|G : K| = n$ . Then*

$$\text{lcm}(m, n) \leq |G : H \cap K| \leq mn, \quad (\text{S1})$$

with the equality (i.e.,  $|G : H \cap K| = mn$ ) realized for  $m, n$  coprime.

*Proof.* First, observe that  $H \cap K$  is a subgroup of both  $H$  and  $K$ , since it is a group and is contained in both  $H$  and  $K$ . Since  $H \cap K \leq H \leq G$ , we have (see 1.3.5 in Ref. [11])

$$|G : H \cap K| = |G : H||H : H \cap K| = m|H : H \cap K|. \quad (\text{S2})$$

Also,  $H \cap K \leq K \leq G$ , thus

$$|G : H \cap K| = |G : K||K : H \cap K| = n|K : H \cap K|. \quad (\text{S3})$$

Hence  $|G : H \cap K|$  is a common multiple of  $m$  and  $n$ , thus  $|G : H \cap K| \geq \text{lcm}(m, n)$ . For the second inequality in Eq. (S1), see 1.3.11(ii) in Ref. [11]; it becomes an equality for  $m, n$  coprime (and  $\text{lcm}(m, n) = mn$  in that case).  $\square$

Finally, we show that the intersection of normal subgroups  $\tilde{\Gamma}^{(1)}$  and  $\tilde{\Gamma}^{(2)}$  corresponding to Abelian clusters can only produce another Abelian cluster. To accomplish this, we rely on the notion of commutator subgroup. The commutator subgroup of a group is generated by all commutators of the group elements. Roughly speaking, the commutator subgroup is a measure of non-commutativity: a large commutator subgroup indicates a ‘less Abelian’ group.

**Lemma I.3.** *Let  $H \triangleleft G$ . Then  $G/H$  is Abelian if and only if  $H$  contains the commutator subgroup  $[G, G] = \langle [g_1, g_2] | g_1, g_2 \in G \rangle$ .*

*Proof.* Denote the (right) coset of  $g_1 \in G$  by  $[g_1] = Hg_1$ . Using the normality of  $H$  in  $G$ , we have:

$$[g_1][g_2] = (Hg_1)(Hg_2) = H(g_1Hg_1^{-1})g_1g_2 = Hg_1g_2. \quad (\text{S4})$$

Likewise,  $[g_2][g_1] = Hg_2g_1$ . Assume that  $G/H$  is Abelian, then  $[g_1][g_2] = [g_2][g_1]$ , which implies  $Hg_1g_2 = Hg_2g_1$ . Multiplying by  $(g_2g_1)^{-1} = g_1^{-1}g_2^{-1}$  from the right, we obtain  $H[g_1, g_2] = H$  where  $[g_1, g_2] = g_1g_2g_1^{-1}g_2^{-1}$  is the commutator of  $g_1$  and  $g_2$ . This implies that  $[g_1, g_2] \in H$  for all  $g_1, g_2 \in G$ , thus  $[G, G] \subseteq H$ .

Now instead, assume  $[G, G] \subseteq H$ . For any  $g_1, g_2 \in G$ , we have:

$$\begin{aligned} [g_1][g_2] &= Hg_1g_2 = Hg_1g_2(g_1^{-1}g_2^{-1}g_2g_1) = H[g_1, g_2]g_2g_1 \\ &= Hg_2g_1 = [g_2][g_1], \end{aligned} \quad (\text{S5})$$

hence  $G/H$  is Abelian. We have used  $H[g_1, g_2] = H$  which holds since  $[g_1, g_2] \in [G, G] \subseteq H$ .  $\square$

**Theorem I.4.** Let  $H, K \triangleleft G$ . Then  $G/H$  and  $G/K$  are both Abelian if and only if  $G/(H \cap K)$  is Abelian.

*Proof.* First assume that  $G/H$  and  $G/K$  are Abelian. By Lemma I.3,  $[G, G]$  is contained in both  $H$  and  $K$ . Thus  $[G, G] \subseteq H \cap K$ , and by the same Lemma,  $G/(H \cap K)$  is Abelian. Now assume instead that  $G/(H \cap K)$  is Abelian. By the same Lemma,  $[G, G]$  is contained in  $H \cap K$ , and thus is contained in both  $H$  and  $K$ . As a result,  $G/H$  and  $G/K$  are both Abelian.  $\square$

Thus, for a cluster constructed from subgroup intersection to be non-Abelian, it is a necessary and sufficient condition that at least one of the two clusters in the intersection is non-Abelian.

We now describe the computational procedure for generating normal subgroups of  $\Gamma$ . We begin with the list of small-index normal subgroups generated by the methods of Ref. [2]. We then randomly select  $n_p$  parent subgroups  $\{\tilde{\Gamma}^{(p)}\}_{p=1}^{n_p}$  among this list with indices between  $N_{\min}$  and  $N_{\max}$ , keeping only the ones with non-Abelian factor groups. We then compute in GAP the intersection

$$\tilde{\Gamma}^{\cap} \equiv \bigcap_{p=1}^{n_p} \tilde{\Gamma}^{(p)} \quad (\text{S6})$$

of the parent subgroups. (Using Lemma I.1 repeatedly, it is clear that  $\tilde{\Gamma}^{\cap}$  thus constructed is normal in  $\Gamma$  for any  $n_p$ .)

If the factor group  $\Gamma/\tilde{\Gamma}^{\cap}$  is of sufficiently large order (i.e., system size), we construct the adjacency matrix for the corresponding non-Abelian PBC cluster. To obtain normal subgroups within some target index range, we have experimented with the input parameters  $(n_p, N_{\min}, N_{\max})$ . We find that input parameters  $(n_p, N_{\min}, N_{\max}) = (2, 15, 20)$  result in  $\tilde{\Gamma}^{\cap}$  with indices  $N \sim 300$ , while  $(n_p, N_{\min}, N_{\max}) = (3, 10, 15)$  gives indices  $N \sim 1500\text{--}2000$ . For our analysis, we randomly chose 13 normal subgroups  $\tilde{\Gamma}^{\cap}$  with indices  $N = \{304, 304, 320, 320, 306, 1560, 1584, 1716, 1800, 1800, 1872, 1980, 1980\}$ , which correspond to the sizes of PBC clusters [see Fig. S1(a)]. The 1D IRs make up 1/2 of all eigenstates in the first four clusters, while the fraction is 1/3 in the other clusters. Note that such indices are completely out of reach of brute-force applications of the low-index normal subgroups procedure, as done e.g. in Refs. [2, 12]. By contrast, the method presented here can, in principle, produce normal subgroups of arbitrarily large indices.

## B. Adjacency matrix

We employ GAP [9] to construct an adjacency matrix  $A$  from a previously obtained normal subgroup  $\tilde{\Gamma}^{\cap}$  with a large index  $N$ . If two elements  $[\eta_n], [\eta_m] \in \Gamma/\tilde{\Gamma}^{\cap}$  correspond to nearest neighbors, they must be related by one of the generators  $\gamma_j$  of  $\Gamma$  [2]:

$$[\eta_n] = [\eta_m][\gamma_j]. \quad (\text{S7})$$

Here, we include  $\{\gamma_1, \gamma_2, \gamma_3, \gamma_4\}$  and their inverses in the generating set:

$$\{\gamma_j\}_{j=1}^8 \equiv \{\gamma_1, \gamma_2, \gamma_3, \gamma_4, \gamma_1^{-1}, \gamma_2^{-1}, \gamma_3^{-1}, \gamma_4^{-1}\}. \quad (\text{S8})$$

The algorithm proceeds through the following steps:

1. Compute the factor group  $\Gamma/\tilde{\Gamma}^{\cap}$ .
2. Compute the right cosets of generators  $\{\gamma_j\}_{j=1}^8$ :
  - (a) Construct the homomorphism  $\Phi : \Gamma \rightarrow \Gamma/\tilde{\Gamma}^{\cap}$  which sends each element  $\eta \in \Gamma$  to the right coset  $[\eta] = \tilde{\Gamma}^{\cap}\eta$ .
  - (b) Compute the right coset  $[\gamma_j] = \Phi(\gamma_j)$  for  $j = 1, \dots, 8$ .
3. Construct the adjacency matrix  $A$ :
  - (a) Initialize  $A$  as an  $N \times N$  matrix with zero entries.
  - (b) For each pair of elements  $[\eta_n], [\eta_m] \in \Gamma/\tilde{\Gamma}^{\cap}$ , if  $[\eta_n] = [\eta_m][\gamma_j]$  for some integer  $j \in [1, 8]$ , then  $[\eta_n]$  and  $[\eta_m]$  are nearest neighbors and we let  $A_{nm} \rightarrow A_{nm} + 1$ . Note that it is possible to have  $A_{nm} \geq 1$ , implying that there are multiple generators relating  $[\eta_n]$  and  $[\eta_m]$ . This is uncommon for large clusters.
4. Construct a matrix  $B$  to record the indices of all the generators that relate a given pair of neighbors:
  - (a) Initialize  $B$  as a three-dimensional  $N \times N \times 8$  array with zero entries.
  - (b) For each pair of elements  $[\eta_n], [\eta_m] \in \Gamma/\tilde{\Gamma}^{\cap}$  and for each index  $j \in [1, 8]$ , if  $[\eta_n] = [\eta_m][\gamma_j]$ , then let  $B_{n,m,j} = 1$ ; otherwise let  $B_{n,m,j} = 0$ .

Step 4 is required for implementing additional on-site degrees of freedom (e.g., orbitals or sublattices), as in the Dirac model (see Section IC).

## C. Hamiltonian construction

The Dirac model on a  $\{8, 8\}$  PBC cluster with  $N$  sites is described by a  $4N \times 4N$  Hamiltonian matrix  $H$ . A 4-component spinor  $\psi$  lives on each site. Nearest-neighboring spinors are coupled by inter-site matrices

$$T_j = \frac{\Gamma_5 - i\Gamma_j}{2}, \text{ for } j = 1, \dots, 4, \quad (\text{S9})$$

and their Hermitian conjugates,

$$T_j = T_{j-4}^\dagger = \frac{\Gamma_5 + i\Gamma_{j-4}}{2}, \text{ for } j = 5, \dots, 8, \quad (\text{S10})$$

where  $\Gamma_\mu = (\Gamma_\mu)^\dagger$  with  $\mu = 1, \dots, 5$  are the Dirac matrices. Given the adjacency matrix  $A$  and the generator-label matrix  $B$  of a PBC cluster, the procedure for defining the Dirac model is as follows:

1. Initialize  $H$  as a  $4N \times 4N$  matrix with zero entries.

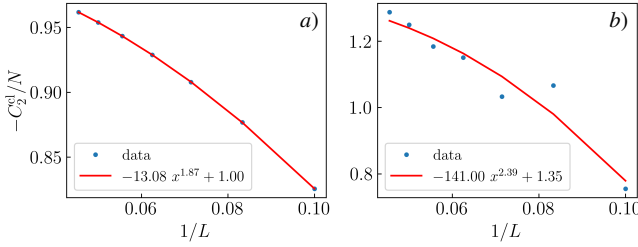


FIG. S2. Scaling of the computed cluster-specific second Chern number  $C_2^{\text{cl}}/N$  as a function of the linear mesh size  $L$  for (a) an Abelian and (b) a non-Abelian cluster with  $N = 16$  primitive cells. The considerable noise in non-Abelian clusters may be attributed to the change in  $C_2$  contribution from different Bloch states that are included at larger  $L$  (smaller  $1/L =: x$ ). Nonetheless, the best-fit curves suggest that, for large  $L$ ,  $-C_2^{\text{cl}}/N$  converges to 1.0 and 1.35, respectively.

2. For each pair of neighboring sites  $n$  and  $m$  such that  $A_{nm} > 0$ , use matrix  $B$  to recall the indices of the generators that relate sites  $n$  and  $m$ . For each recalled index  $j'$ , add to  $H$  the tensor product of  $M$ , which is a  $N \times N$  matrix with zeros everywhere except at  $M_{nm} = 1$ , and  $T_{j'}$ :

$$H \rightarrow H + M \otimes T_{j'}. \quad (\text{S11})$$

3. To add a nonzero mass  $m$ , add to  $H$  the tensor product of the identity matrix  $I_{N \times N}$  and  $\Gamma_5$ :

$$H \rightarrow H + mI_{N \times N} \otimes \Gamma_5. \quad (\text{S12})$$

The DOS for  $H$  thus constructed is shown for various PBC clusters and compared with  $U(1)$ -HBT in Fig. S1(a).

#### D. Flux insertion

To explore the topological response of finite systems to external fields, we focus on small PBC clusters and compute the cluster-specific second Chern number  $C_2^{\text{cl}}$  by threading fluxes along the four translation directions. Namely, we append a phase to the inter-site transition matrices  $T_j$  in Eq. (S9) as  $T_j \rightarrow T_j e^{i\phi_j}$  with  $\phi = \{\phi_j\}_{j=1}^4 \in [0, 2\pi]^4$ . We consider Abelian and non-Abelian clusters with  $N = 16, 18, 20$  primitive cells. For the non-Abelian clusters, the non-Abelian states constitute 1/2, 2/3, and 4/5 of the total eigenstates, respectively.

In the flux space, the total second Chern number of a multiplet of  $n_f$  filled bands (which may have mutual degeneracies) is [13]

$$C_2 = \frac{1}{32\pi^2} \int_{\mathbb{T}^4} d^4\phi \epsilon^{jklm} \text{Tr}(F_{jk}F_{lm}), \quad (\text{S13})$$

where

$$F_{jk} = \frac{\partial A_k}{\partial \phi_j} - \frac{\partial A_j}{\partial \phi_k} + i[A_j, A_k] \quad (\text{S14})$$

is the non-Abelian Berry curvature in the plane spanned by directions  $j$  and  $k$ , and

$$A_j^{\alpha\beta} = \langle \psi_\alpha(\phi) | \frac{\partial}{\partial \phi_j} | \psi_\beta(\phi) \rangle \quad (\text{S15})$$

is the non-Abelian Berry connection computed from eigenstates  $|\psi_\alpha(\phi)\rangle$  with  $\alpha = 1, \dots, n_f$ . Here  $\epsilon^{jklm}$  is the Levi-Civita symbol in 4D with an implicit sum over repeated indices and the integration is over the 4-torus  $\mathbb{T}^4$  defined by  $\phi$ . We follow Ref. 14 for the numerical computation of  $C_2$ .

Let us remark that while for the computation of first Chern number  $C_1$  on a 2D manifold there exists an elegant algorithm of Ref. 15 that guarantees the correct quantized result for a rather coarse choice of a momentum-space grid (namely, the only requirement to find the correct integer is that the Berry phase on each square of the grid is less than  $\pi$ ), the algorithm of Ref. 14 to compute second Chern number  $C_2$  exhibits deviations from the correct results for any finite momentum-space grid. Therefore, we study the dependence of the numerically computed  $C_2^{\text{cl}}$  on the grid size  $L$  in Fig. S2 to find the result extrapolated at  $L \rightarrow \infty$ . Our results show that while the Abelian clusters have  $C_2^{\text{cl}}/N = C_2$  in agreement with the band theory, positioning of the Bloch states with respect to the nodal manifold influences  $C_2^{\text{cl}}$  in non-Abelian clusters. Our implementation of the numerical algorithm is available in the Supplementary Data and Code [16].

## II. $U(d)$ -HBT

Here we provide details about the algorithm for sampling  $\text{BZ}^{(1,d)}$ . We focus on the simplest class of non-Abelian Bloch states, i.e.,  $(d = 2)$ -dimensional irreducible representations, where the matrices  $U_j$ ,  $j = 1, \dots, 4$  belong to the  $SU(2)$  group. In Fig. S1(b), the data for  $SU(3)$  are obtained by nearly identical steps, with the only difference being the matrix dimension and parameterization.

In general, an  $SU(2)$  matrix may be parameterized as

$$U_j = \begin{pmatrix} a_j & b_j \\ -b_j^* & a_j^* \end{pmatrix}, \quad (\text{S16})$$

where  $a_j, b_j \in \mathbb{C}$  and  $|a_j|^2 + |b_j|^2 = 1$ . The latter condition reduces the number of free real parameters to three. To be a valid representation of the Fuchsian group  $\Gamma$ , one has to ensure that the choice of four matrices  $U$  obey

$$U_1 U_2^{-1} U_3 U_4^{-1} U_1^{-1} U_2 U_3^{-1} U_4 - \mathbb{1}_2 = 0. \quad (\text{S17})$$

The procedure to find solutions  $\{U_j\}_{j=1}^4 \equiv U$  is as follows. We pick random  $U_{1,2}$  according to the circular unitary ensemble, which represents a uniform distribution over the unitary  $d \times d$  matrices, and corresponds to the Haar measure on the unitary group. Subsequently, we choose a random initial choice of  $U_{3,4}$  according to the same uniform distribution, which we decompose into  $a_{3,4}$  and  $b_{3,4}$  per Eq. (S16), and we perform a gradient descent with respect to these parameters to minimize the Frobenius norm of Eq. (S17). Sometimes, this procedure gets trapped in a local minimum that does not solve Eq. (S17); in

that case the matrices are discarded and we repeat the steps for a different choice of fixed  $U_{1,2}$  and initial  $U_{3,4}$ . The algorithm is iterated until we reach a specified number of solutions  $\mathbf{U}$ .

To motivate why our described approach for finding random representations  $\mathbf{U}$  works, let us discuss the dimensions of the mathematical spaces at play. First, the space of *distinct*  $d$ -dimensional (unitary) representations  $D_\lambda$  of  $\Gamma$ , i.e., where equivalent representations are treated as a single point, is called the  $U(d)$ -character variety  $X(\Sigma_2, U(d))$ ; here,  $\Sigma_2$  is the genus-2 surface obtained from compactifying the edges of the primitive cell of the  $\{8, 8\}$  lattice. This variety is known to be ten-dimensional [2, 17]. One can further decompose the representation matrices on the group generators as  $D_\lambda(\gamma_j) = U_j e^{ik_j}$ , where  $e^{ik_j} \in U(1)$  and  $U_j \in SU(2)$ . The  $U(1)$  factors clearly absorb four of the ten dimensions of  $X(\Sigma_2, U(2))$ , implying that the space of non-equivalent  $SU(2)$  representation matrices that obey Eq. (S17) is six-dimensional.

Crucially, in our numerical search for random  $SU(2)$  matrices obeying Eq. (S17) we also need to account for distinct choices of representation matrices  $\mathbf{U}$  that fall into the same equivalence class. Recall that given a unitary matrix  $M$ , the choice  $MUM^\dagger$  constitutes a representation of  $\Gamma$  that is *equivalent* to  $\mathbf{U}$  as it merely corresponds to a unitary rotation of the eigenvectors of the Hamiltonian  $H_\lambda^{(1,d)}$  that span the representation. However, our numerical search is not restricted from potentially finding equivalent representations. Since the  $SU(2)$  group is three-dimensional, the orbit  $\cup_{M \in SU(2)} MUM^\dagger$  of the set  $\{U_j\}_{j=1}^4$  is generically three-dimensional; consequently, such unitary transformations increase the extent of  $SU(2)$  solutions  $\mathbf{U}$  to Eq. (S17) to a nine-dimensional manifold. By selecting a randomly chosen  $U_{1,2}$ , we fix six of the nine parameters; in other words, the space of solutions for  $U_{3,4}$  with given  $U_{1,2}$  (if such solutions exist) is generically three-dimensional. We verified that by performing minimization of the Frobenius norm of Eq. (S17) for different initial choices of  $U_{3,4}$  and fixed  $U_{1,2}$  we obtain different optimized solutions for  $U_{3,4}$ . Note that finding solutions for  $U_4$  given randomly chosen  $U_{1,2,3}$ , which corresponds to fixing nine coordinates, generically does *not* yield any result. This is because the orbit of a single matrix  $\cup_{M \in SU(2)} MU_j M^\dagger$  can be shown to be only two-dimensional. As a consequence, fixing three random matrices  $U_{1,2,3}$  already overdetermines the problem of finding  $U_4$ .

Before concluding, let us make three final remarks. First, to make sure that we investigate all *dimensions* of BZ $^{(1,d)}$  uniformly, we compute the Hamiltonian spectrum for  $L^6 \times L^4 = L^{10}$  unitary representations; here,  $L^6$  points correspond to the random choice of  $SU(2)$  matrices  $\mathbf{U}$  inside the six-dimensional space of distinct representations, and  $L^4$  corresponds to choices of  $U(1)$  factors  $\{e^{ik_j}\}_{j=1}^4$  inside the four-dimensional space of momenta. For the presented data, we chose  $L = 8$ . Second, owing to the lack of explicit parametrizations of these higher BZs, it is presently unknown to us whether they are equipped with a canonical measure of volume. Therefore, it is possible that our random sampling is non-homogeneous, i.e., it explores some sectors more densely than others. Despite these subtleties, the good agreement of  $U(2)$ -HBT and 2-supercell DOS lends support to the outlined scheme. Finally, when generalizing the algorithm to  $SU(3)$  matrices, the decomposition in Eq. (S16)

has to be replaced by an eight-parameter decomposition, as shown in Ref. [18]. A comparison of DOS computed from randomly sampled 2D and 3D representations is shown in Fig. S1(b).

We note in passing that while  $U(d)$ -HBT on the primitive cell and  $U(1)$ -HBT on  $n$ -supercells provide complementary ways to access the non-Abelian states, an investigation of  $U(d)$  Bloch theory on  $n$ -supercells could conceivably open up a larger share of the hyperbolic reciprocal space. We did not pursue such a generalization in this work.

### III. SUPERCELL METHOD

#### A. Hyperbolic translation groups

As described in the main text, the supercell method [19] applies  $U(1)$ -HBT to supercells in order to gain access to the non-Abelian BZs. By considering sequences of supercells with increasing number  $n$  of primitive cells, an increasing number of non-Abelian Bloch states is generated and convergence is achieved for  $n \rightarrow \infty$ . Supercells can be defined [19] in terms of factor groups  $G$  of the underlying space group (more precisely its proper subgroup) with a translation group  $\Gamma$ . The proper subgroup of the space group of the  $\{8, 8\}$  lattice is the proper triangle group with presentation

$$\Delta^+(2, 8, 8) = \langle x, y, z | x^2, y^8, z^8, xyz \rangle, \quad (\text{S18})$$

generated by rotations  $x$ ,  $y$ , and  $z$  around the three vertices of a hyperbolic triangle by angles  $\frac{2\pi}{2}$ ,  $\frac{2\pi}{8}$ , and  $\frac{2\pi}{8}$ , respectively, which satisfy the constraints that the products listed after the vertical line are equal to the identity (Fig. S3).

To achieve convergence to the thermodynamic limit [3, 20], the sequence of translation groups  $\Gamma^{(\ell)} \triangleleft \Delta^+$  with  $\ell \in \{1, 2, 3, \dots\}$  needs to obey the normal subgroup relations

$$\Gamma^{(1)} \triangleright \Gamma^{(2)} \triangleright \dots \triangleright \Gamma^{(\ell)} \triangleright \dots, \quad (\text{S19})$$

such that  $\bigcap_{\ell \geq 1} \Gamma^{(\ell)}$  is the trivial group containing only the identity element [3]. Note that in the main text we used a slightly different notation, where the superscript  $^{(n)}$  of a translation subgroup indicates its subgroup index

$$n = |\Gamma : \Gamma^{(\ell)}|, \quad (\text{S20})$$

whereas here the superscript  $^{(\ell)}$  denotes the position of the subgroup in the coherent sequence (S19). This distinction is of little importance in the main text, since we take the second element ( $\ell = 2$ ) in Eq. (S19) to be a 2-supercell ( $n = 2$ ).

The  $n$ -supercell is compactified into a surface of genus  $g^{(n)}$  that grows linearly with  $n$ , as expressed by the Riemann-Hurwitz formula [21]. Specifically, if  $g_{pc}$  is the genus of the compactified primitive cell, then  $g^{(n)} = n(g_{pc} - 1) + 1$ . Here, we adopt the same sequence that was considered in Ref. [19] for the nearest-neighbor hopping model on the  $\{8, 8\}$  lattice. This sequence was obtained from the factor groups given in Ref. [22] using the HYPERBLOCH package [23] and they are denoted by T2.6, T3.11, T5.13, T9.20, T17.29, T33.44, where

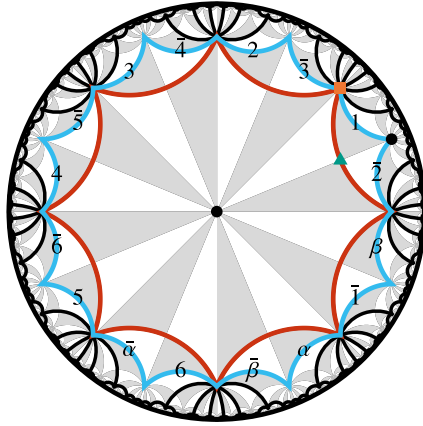


FIG. S3. Symmetries and unit cells of the  $\{8,8\}$  lattice. The space group symmetries of the lattice are illustrated by grey and white triangles which are generated by applying those symmetry operations to a single one of them. Both the symmetric primitive cell (red polygon) as well as the symmetric 2-supercell (blue polygon), consisting of two copies of the primitive cell, are shown. The boundary identification of the supercell is indicated as follows: the edge labeled  $\bar{j}$  is related to the edge labeled  $j$  by the translation generator  $\gamma_j \in \Gamma^{(2)}$ . Edges related by composite translations are labeled by  $\bar{\alpha}$ ,  $\alpha = \gamma_3^{-1}\gamma_1^{-1}$ , and  $\bar{\beta}$ ,  $\beta = \gamma_4^{-1}\gamma_2^{-1}$ . For the purpose of Appendix III C 3, we indicate the following high-symmetry positions. Black dots mark inversion centers with respect to sites of the  $\{8,8\}$  lattice, green triangle with respect to mid-edge, and orange square with respect to faces of the lattice.

“ $Tg.j$ ” labels the  $j^{\text{th}}$  quotient of any triangle group  $\Delta^+(r, q, p)$  where the quotient acts on a surface of genus  $g$ . Their explicit presentations are

$$\begin{aligned} G^{(1)} &= \langle x, y, z \mid x^2, y^8, z^8, xyz, xzy, y^3z^{-1} \rangle, \\ G^{(2)} &= \langle x, y, z \mid x^2, y^8, z^8, xyz, xzy \rangle, \\ G^{(3)} &= \langle x, y, z \mid x^2, y^8, z^8, xyz, xy^{-2}z^{-1}y, xzy^{-1}z^{-2} \rangle, \\ G^{(4)} &= \langle x, y, z \mid x^2, y^8, z^8, xyz, xy^{-2}z^{-1}y \rangle, \\ G^{(5)} &= \langle x, y, z \mid x^2, y^8, z^8, xyz, xzy^{-2}z^{-2}y, (yz^{-1}y^2)^2 \rangle, \\ G^{(6)} &= \langle x, y, z \mid x^2, y^8, z^8, xyz, xzy^{-2}z^{-2}y \rangle. \end{aligned} \quad (\text{S21})$$

The 2-supercell derived from  $G^{(2)}$  including boundary identifications is illustrated in Fig. S3. For each  $n$ -supercell, we construct the U(1) Bloch Hamiltonian  $H_{\mathbf{k}}^{(n,1)}$ , parameterized by the momentum vector  $\mathbf{k} \in \text{BZ}^{(n,1)} \cong \mathbb{T}^{2g^{(n)}}$ .

## B. Hyperbolic Brillouin zones

Because of the subgroup relations in Eq. (S19), one can always express supercell translation generators in terms of  $\{\gamma_1, \gamma_2, \gamma_3, \gamma_4\}$  and their inverses. For the 2-supercell, specifically, we find

$$\begin{aligned} \tilde{\gamma}_1 &= \gamma_4\gamma_1, & \tilde{\gamma}_2 &= \gamma_1^{-1}\gamma_2, \\ \tilde{\gamma}_3 &= \gamma_2^{-1}\gamma_3, & \tilde{\gamma}_4 &= \gamma_3^{-1}\gamma_4, \\ \tilde{\gamma}_5 &= \gamma_4^{-1}\gamma_1^{-1}, & \tilde{\gamma}_6 &= \gamma_1\gamma_2^{-1}. \end{aligned} \quad (\text{S22})$$

These relations among the translation generators imply the following immersion of the original 4D  $\text{BZ}^{(1,1)}$  inside the 6D  $\text{BZ}^{(2,1)}$ :

$$\begin{aligned} \iota : \quad \text{BZ}^{(1,1)} &\rightarrow \text{BZ}^{(2,1)} \\ (k_1, k_2, k_3, k_4) &\mapsto (k_4 + k_1, k_2 - k_1, k_3 - k_2, k_4 - k_3, -k_4 - k_1, k_1 - k_2) \end{aligned} \quad (\text{S23})$$

Note that the immersion  $\iota$  is not one-to-one (i.e., it is non-injective): two four-momenta that differ by  $\pi$  in all components  $\{k_j\}_{j=1}^4$  are mapped onto the same six-momentum in  $\text{BZ}^{(2,1)}$ . This two-to-one mapping (associated with doubling of the number of bands) is analogous to the Brillouin-zone folding that accompanies supercell constructions in Euclidean lattices. We also remark that the immersion  $\iota(\text{BZ}^{(1,1)})$  passes through the point  $(0, 0, 0, 0, 0, 0)$  of  $\text{BZ}^{(2,1)}$ , which corresponds to the center of the nodal-line ring derived in Sec. III C 1. For this reason, the second Chern number computed inside  $\text{BZ}^{(1,1)}$  relates to the second Chern number associated with the nodal ring inside  $\text{BZ}^{(2,1)}$ .

By randomly sampling  $\text{BZ}^{(n,1)}$  with  $10^9$   $\mathbf{k}$ -points and diagonalizing  $H_{\mathbf{k}}^{(n,1)}$  for each of them, we compute the energy spectrum. The DOS is then obtained with an energy resolution of 0.005 [Fig. S1(c)]. The appearance of peaks in the DOS may be understood as a consequence of “band folding”, which increases the number of energy bands. We observe convergence with increasing supercell size  $n$ . Crucially, the DOS near zero energy converges rapidly, such that already the 2-supercell (T3.11) gives a good approximation. Therefore, we next study the corresponding Bloch Hamiltonian  $H_{\mathbf{k}}^{(2,1)}$  on the 6D  $\text{BZ}^{(2,1)}$ .

Before narrowing our attention to the 2-supercell Bloch Hamiltonian in Sec. III C 1, let us briefly comment on the existence of a general subset relation

$$\text{BZ}^{(n_\ell, d)} \subset \text{BZ}^{(n_{\ell+1}, d)} \quad (\text{S24})$$

which generalizes the particular immersion in Eq. (S23). This sought relation follows directly from the subgroup relation  $\Gamma^{(\ell)} < \Gamma^{(\ell+1)}$  between the translation groups. Namely, if  $\lambda$  is a  $d$ -dimensional representation of  $\Gamma^{(\ell)}$  that for  $g \in \Gamma^{(\ell)}$  assigns  $g \mapsto \lambda(g)$ , then a restriction of this mapping to  $g \in \Gamma^{(\ell+1)}$  gives a *subduced representation* of  $\Gamma^{(\ell+1)}$  [19]. This subduction defines the immersion (and therefore a subset relation) among the spaces  $\text{BZ}^{(n_\ell, d)}$  and  $\text{BZ}^{(n_{\ell+1}, d)}$  of  $d$ -dimensional representations. Note that this immersion is not injective, because different representations  $\lambda_1 \neq \lambda_2$  of  $\Gamma^{(\ell)}$  may subduce the same representation  $\lambda$  when restricted to elements of the subgroup  $\Gamma^{(\ell+1)}$ . For example, we already showed that the immersion in Eq. (S23) is two-to-one.

### C. 2-supercell approximation

#### 1. Abelian Bloch Hamiltonian for 2-supercells

The Bloch Hamiltonian corresponding to the 2-supercell can be expressed as a linear combination of  $8 \times 8$  matrices as

$$H_{\mathbf{k}}^{(2,1)} = \frac{1}{4} \sum_{ij\ell} d_{ij\ell} \sigma_{ij\ell}, \quad (\text{S25})$$

where  $\sigma_{ij\ell} = \sigma_i \otimes \sigma_j \otimes \sigma_\ell$ , with  $\{\sigma_i\}_{i=0}^3$  denoting the Pauli matrices and the  $2 \times 2$  identity matrix. The non-zero summands in Eq. (S25) are

$$d_{0,3,3} = 4m, \quad (\text{S26a})$$

$$d_{1,1,0} = -ie^{-i(k_2+k_3+k_4+k_5)} \left( -1 + e^{2i(k_2+k_3+k_4+k_5)} \right), \quad (\text{S26b})$$

$$d_{1,2,0} = -ie^{-i(k_2+k_3+k_4+k_5+k_6)} \left( -1 + e^{i(k_3+k_4+k_5+k_6)} \right) \left( 1 + e^{i(2k_2+k_3+k_4+k_5+k_6)} \right), \quad (\text{S26c})$$

$$d_{1,3,1} = ie^{-i(k_1+k_2+k_3+k_4+k_6)} \left( e^{i(k_1+k_3)} - e^{i(k_4+k_6)} \right) \left( e^{ik_1} + e^{i(2k_2+k_3+k_4+k_6)} \right), \quad (\text{S26d})$$

$$d_{1,3,2} = ie^{-i(k_1+k_2+k_3+k_4)} \left( e^{ik_1} + e^{i(k_2+k_3+k_4)} \right) \left( -1 + e^{i(k_1+k_2+k_3+k_4)} \right), \quad (\text{S26e})$$

$$\begin{aligned} d_{1,3,3} = & e^{-i(k_1+k_2+k_3+k_4+k_5+k_6)} \left( e^{ik_1} + e^{i(2k_1+k_3+k_5)} + e^{i(k_1+k_6)} + e^{i(k_1+k_5+k_6)} + e^{i(k_1+k_4+k_5+k_6)} \right. \\ & + e^{i(k_1+k_3+k_4+k_5+k_6)} + e^{i(k_2+k_3+k_4+k_5+k_6)} + 2e^{i(k_1+k_2+k_3+k_4+k_5+k_6)} + e^{i(2k_1+k_2+k_3+k_4+k_5+k_6)} \\ & + e^{i(k_1+2k_2+k_3+k_4+k_5+k_6)} + e^{i(k_1+2k_2+2k_3+k_4+k_5+k_6)} + e^{i(k_1+2k_2+2k_3+2k_4+k_5+k_6)} \\ & \left. + e^{i(k_1+2k_2+2k_3+2k_4+2k_5+k_6)} + e^{i(2k_2+k_3+2k_4+k_5+2k_6)} + e^{i(k_1+2(k_2+k_3+k_4+k_5+k_6))} \right), \end{aligned} \quad (\text{S26f})$$

$$d_{2,1,0} = -e^{-i(k_2+k_3+k_4+k_5)} \left( -1 + e^{i(k_2+k_3+k_4+k_5)} \right)^2, \quad (\text{S26g})$$

$$d_{2,2,0} = -e^{-i(k_2+k_3+k_4+k_5+k_6)} \left( -1 + e^{i(k_3+k_4+k_5+k_6)} \right) \left( -1 + e^{i(2k_2+k_3+k_4+k_5+k_6)} \right), \quad (\text{S26h})$$

$$d_{2,3,1} = e^{-i(k_1+k_2+k_3+k_4+k_6)} \left( e^{i(k_1+k_3)} - e^{i(k_4+k_6)} \right) \left( e^{i(2k_2+k_3+k_4+k_6)} - e^{ik_1} \right), \quad (\text{S26i})$$

$$d_{2,3,2} = e^{-i(k_1+k_2+k_3+k_4)} \left( e^{i(k_2+k_3+k_4)} - e^{ik_1} \right) \left( -1 + e^{i(k_1+k_2+k_3+k_4)} \right), \quad (\text{S26j})$$

$$\begin{aligned} d_{2,3,3} = & ie^{-i(k_1+k_2+k_3+k_4+k_5+k_6)} \left( e^{ik_1} + e^{i(2k_1+k_3+k_5)} + e^{i(k_1+k_6)} + e^{i(k_1+k_5+k_6)} + e^{i(k_1+k_4+k_5+k_6)} \right. \\ & + e^{i(k_1+k_3+k_4+k_5+k_6)} - e^{i(k_2+k_3+k_4+k_5+k_6)} + e^{i(2k_1+k_2+k_3+k_4+k_5+k_6)} - e^{i(k_1+2k_2+k_3+k_4+k_5+k_6)} \\ & - e^{i(k_1+2k_2+2k_3+k_4+k_5+k_6)} - e^{i(k_1+2k_2+2k_3+2k_4+k_5+k_6)} - e^{i(k_1+2k_2+2k_3+2k_4+2k_5+k_6)} \\ & \left. - e^{i(2k_2+k_3+2k_4+k_5+2k_6)} - e^{i(k_1+2(k_2+k_3+k_4+k_5+k_6))} \right). \end{aligned} \quad (\text{S26k})$$

As we shall see in the next section, symmetries constrain some

of the nodes to lie in the  $(k_a, k_b, -k_a, -k_b, k_a, k_b)$  plane for

$k_{a,b} \in [-\pi, +\pi]$ . To obtain the low-energy spectrum in this plane and to simplify the expressions, we proceed in three steps:

1. A basis transformation on the Bloch Hamiltonian makes the structure of the ring manifest in the small momentum expansion:  $\tilde{H}_{\mathbf{k}}^{(2,1)} = V_H H_{\mathbf{k}}^{(2,1)} V_H^\dagger$ , with  $V_H = \text{diag}(1, 1, 1, 1, r, r, r, r)$  and  $r = e^{i(k_1 - k_2)/2}$ .

2. For a direct handle on the nodal plane, we perform a basis rotation to obtain the Hamiltonian  $\tilde{H}_{\mathbf{q}}^{(2,1)}$  where  $\mathbf{q} = V_{\mathbf{k}} \mathbf{k}$  and

$$V_{\mathbf{k}} = \frac{1}{\sqrt{6}} \begin{pmatrix} \sqrt{2} & 0 & \sqrt{3} & 0 & -1 & 0 \\ 0 & \sqrt{2} & 0 & \sqrt{3} & 0 & -1 \\ -\sqrt{2} & 0 & \sqrt{3} & 0 & 1 & 0 \\ 0 & -\sqrt{2} & 0 & \sqrt{3} & 0 & 1 \\ \sqrt{2} & 0 & 0 & 0 & 2 & 0 \\ 0 & \sqrt{2} & 0 & 0 & 0 & 2 \end{pmatrix}. \quad (\text{S27})$$

Essentially,  $V_{\mathbf{k}}$  provides an orthonormal basis where the first two columns span the nodal plane and the ring now lies in  $(q_1, q_2, 0, 0, 0, 0)$ . At this stage, to leading order in momenta  $\mathbf{q}$ , the Hamiltonian near the origin is given by  $\tilde{H}_{\mathbf{q}}^{(2,1)} = \sum_{ij\ell} d_{ij\ell} \sigma_{ij\ell}$  and

$$d_{0,3,3} = m, \quad (\text{S28a})$$

$$d_{1,3,3} = -\frac{q_1^2 + q_2^2}{6} + 4, \quad (\text{S28b})$$

$$d_{1,1,0} = \frac{q_3 + 2q_4 + \sqrt{3}q_5}{2\sqrt{2}}, \quad (\text{S28c})$$

$$d_{1,2,0} = \frac{q_3 + q_4 + \sqrt{3}(q_5 + q_6)}{2\sqrt{2}}, \quad (\text{S28d})$$

$$d_{1,3,1} = \frac{-2q_3 + q_4 + \sqrt{3}q_6}{2\sqrt{2}}, \quad (\text{S28e})$$

$$d_{1,3,2} = -\frac{q_3 + q_4}{\sqrt{2}}, \quad (\text{S28f})$$

$$d_{2,3,3} = \frac{3(q_3 + q_4) + \sqrt{3}(q_5 + q_6)}{\sqrt{2}}. \quad (\text{S28g})$$

Note that the nodal ring lies in the plane spanned by  $(q_1, q_2)$  and its form is apparent in  $d_{1,3,3}$ . The terms Eq. (S28)(b–f) form a set of mutually anti-commuting matrices. The eigenvalues in this low-energy approximation are given by

$$E^2 = \frac{1}{36} \left( q_1^2 + q_2^2 - 24 \right)^2 + m^2 + X^2 + d_{2,3,3}^2 \quad (\text{S29})$$

$$\pm 2\sqrt{m^2 \left( d_{2,3,3}^2 + (q_1^2 + q_2^2 - 24)^2 / 36 \right) + d_{2,3,3}^2 X^2},$$

wherein  $X^2 = d_{1,1,0}^2 + d_{1,2,0}^2 + d_{1,3,1}^2 + d_{1,3,2}^2$  and each of the four energy bands is doubly degenerate.

3. To proceed, it would be convenient to diagonalize the expression  $X$ , i.e., identify an orthonormal basis for the coordinates  $(q_3, q_4, q_5, q_6)$ , while leaving  $(q_1, q_2)$  unaltered. By obtaining the eigenvectors of the matrix representation of  $X$ , it can be shown that with

$$\begin{pmatrix} q_3 \\ q_4 \\ q_5 \\ q_6 \end{pmatrix} \rightarrow \frac{1}{4} \begin{pmatrix} 2\alpha_+ & 2\beta_+ & 2\alpha_- & 2\beta_- \\ -\kappa_+ & \kappa_- & \kappa_- & \kappa_+ \\ \kappa_- & -\kappa_+ & \kappa_+ & \kappa_- \\ 2\alpha_- & -2\beta_- & -2\alpha_+ & 2\beta_+ \end{pmatrix} \begin{pmatrix} q_3 \\ q_4 \\ q_5 \\ q_6 \end{pmatrix}, \quad (\text{S30})$$

such that  $\alpha_{\pm} = \sqrt{1 \pm \frac{1}{2\sqrt{19}}}$ ,  $\beta_{\pm} = \sqrt{1 \pm \frac{7}{2\sqrt{19}}}$  and  $\kappa_{\pm} = \sqrt{3} \pm 1$ , one has

$$4X^2 = \left( 5 + \sqrt{19} \right) q_3^2 + \left( 3 + \sqrt{3} \right) q_4^2 + \left( 3 - \sqrt{3} \right) q_5^2 + \left( 5 - \sqrt{19} \right) q_6^2. \quad (\text{S31})$$

From Eq. (S29), the energy vanishes when

$$4X^2 = - \left( (q_1^2 + q_2^2 \pm 24) / 6 \pm \sqrt{m^2 - d_{2,3,3}^2} \right)^2, \quad (\text{S32})$$

which in turn implies that  $X = 0$ ,  $q_3 = q_4 = q_5 = q_6 = 0$  and  $d_{2,3,3} = 0$ . It is then easy to deduce that the nodal line is described by  $q_1^2 + q_2^2 = 6(4 - |m|)$ .

## 2. Mass dependence of the nodal manifold

The nodal manifold of the 2-supercell in its 6D BZ can be further studied as a function of the mass  $m$ . As seen in Fig. S4, the manifold has a complicated structure when projected to the first three momentum coordinates. The simple structure of a nodal ring emerges only close to  $m = 3$ . Referring to the case of Weyl semimetals, the degeneracy in the spectrum can only be removed either by breaking translation symmetry and allowing the Weyl points to hybridize or by tuning model parameters to bring them together. Similarly, here the nodal ring shrinks to a point as one tunes the mass towards  $m = 4$ , which marks a phase transition to the trivial atomic limit.

The topology characterizing the nodal line can be visualized by integrating the second Chern number for fixed  $(k_1, k_2)$  (the horizontal coordinates of plots in Fig. S4) along the four-dimensional torus spanned by the remaining momenta  $(k_3, k_4, k_5, k_6)$ . For  $m = 3$  the computed  $C_2$  data exhibits a clear convergence; therefore, we carry the integration for a single grid size  $L = 15$  and round the result to the nearest integer. The outcome of this computation is plotted in the horizontal plane of Fig. 3(b) of the main text. In addition, we attempted to perform an analogous computation for  $m = 2.5$ , where the data in Fig. S4 suggest eleven distinct nodal-line rings. The occurrence of multiple nodal lines implies that the typical gap size on the four-dimensional tori is smaller, making the Berry curvature peaks sharper, thus necessitating a finer momentum-space grid. We show in Fig. S5(a) the result of the integration for the grid size  $L = 15$ , where large deviations from quantized values are observed. Therefore, following the discussion in Sec. ID, we perform the computation for a range of grid sizes  $L \in \{5, 6, \dots, 12, 13, 15\}$  and then perform a finite-size scaling with the fitting function

$$C_2 = C_{2,\infty} + \frac{a}{L} + \frac{b}{L^2}. \quad (\text{S33})$$

Unfortunately, the considered range of grid sizes  $L$  turns out to be insufficient for extracting well converged results. Namely, in Fig. S5(b) we plot the extract values of  $C_{2,\infty}$  where significant noise is observed. Due to computational limitations we did not perform the analysis with larger values of  $L$  and for smaller  $|m|$ .

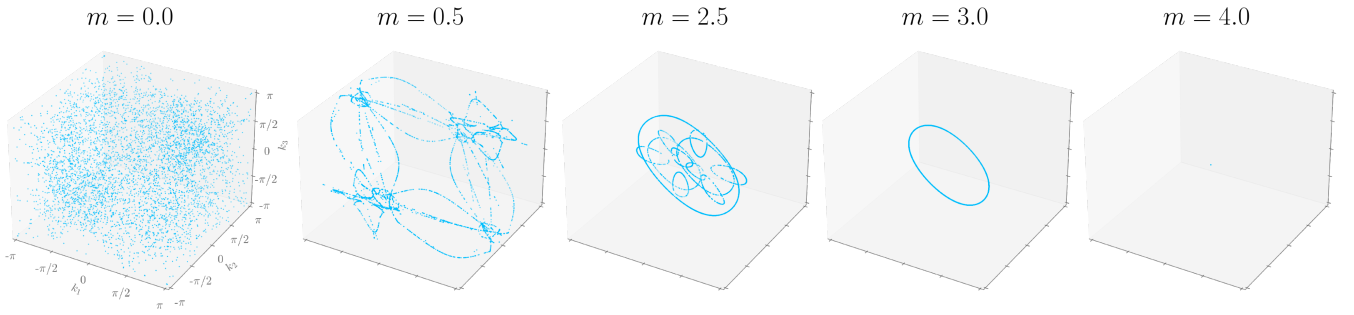


FIG. S4. Evolution of the nodal manifold within the 2-supercell description as a function of mass  $m$ . Each point denotes a projected six-momentum coordinate where the spectral gap at half-filling vanishes. The nodal ring emerges close to  $m = 3$ , shrinks to a point at the origin when  $m = 4$ , and finally vanishes as the system enters the trivial insulating phase. The behavior is mirrored for negative values of the mass.

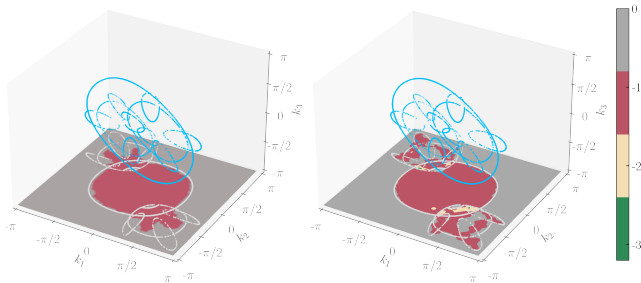


FIG. S5. Second Chern number  $C_2$  of the 2-supercell Hamiltonian at mass parameter  $m = 2.5$ , computed by integration inside the four-dimensional tori with fixed momenta  $(k_1, k_2)$  for (a)  $L = 15$  and (b) when extrapolated to large  $L$  by rounding  $C_{2,\infty}$  in the fitted function (S33) to the nearest integer. The data is noisy due to computational limitations.

We next extract the scaling of the DOS as a function of the energy, with the result displayed in Fig. S6. Assuming a power-law scaling of the DOS close to  $E = 0$ , i.e.  $\rho(E \rightarrow 0) \propto E^\alpha$ , we fit the data using a non-linear least-squares algorithm. To account for the non-normally distributed errors in the data obtained from random sampling, we perform a weighted least-squares fit with weights given by the inverse square-root of the *observed* DOS values (see Section III D for more details on the fitting procedure). We find good agreement with the model  $\rho(E) \propto E^\alpha$  when fitting in an energy range of width  $E_{\max} - E_{\min} = 0.1$ , starting from the lowest energy  $E_{\min} > 0$  for which the DOS data does not exhibit any holes (i.e., energy bins with no sampled states). The extracted scaling exponent  $\alpha$  varies with  $0 < m \leq 4$  within the range  $(3.3, 4.1)$ . For  $0 < m < 3$ , a deviation to values somewhat smaller than the theoretically predicted  $\alpha = 4$  (see Section III C 3) is observed, while it remains closer to 4 in the range  $3 \leq m \leq 4$ . Exactly at  $m = 0$ , however, the 2-supercell DOS has a linear scaling,  $\alpha = 0.976 \pm 0.002$ . On the other hand, for  $m > 4$ , a gap opens in the 2-supercell spectrum and  $\alpha$ , as extracted with our fitting procedure, suddenly jumps from roughly 3.8 at  $m = 4$  to  $30 \pm 1$  at  $m = 4.25$ .

### 3. Symmetry protection of the nodal ring

In this section, we analyze how certain crystalline symmetries of the hyperbolic  $\{8, 8\}$  lattice impose particular band-structure features observed inside the 6D  $BZ^{(2,1)}$  of the 2-supercell Hamiltonian discussed in Appendix III C 1. Special attention is given to space inversion ( $\mathcal{P}$ ) and to time reversal ( $\mathcal{T}$ ). In particular, these symmetries allow us to address the three following aspects: (i) identify the 2D plane of the nodal ring, which is enforced by inversion of bands with opposite  $\mathcal{P}$ -inversion eigenvalues, (ii) clarify the two-fold Kramers degeneracy of all bands, and (iii) explain the codimension  $\mathfrak{d} = 5$  for node formation at generic values of  $m$  as well as the significantly decreased codimension  $\mathfrak{d} = 2$  observed for  $m = 0$ .

Let us begin by discussing the role of  $\mathcal{PT}$  symmetry in the 4D  $BZ^{(1,1)}$  of the hyperbolic Bloch Hamiltonian  $H_k^{(1,1)}$  constructed on the primitive unit cell, which matches exactly the Bloch Hamiltonian of the 4D QHI on a hypercubic lattice [13, 24]. The topology of the latter Hamiltonian is well understood [25]. In particular, it is easily verified that  $H_k^{(1,1)}$  in Eq. (3)) commutes with  $\mathcal{PT} = \mathbb{F}_2 \mathbb{F}_4 \mathcal{K}$ :

$$(\mathcal{PT}) H_k^{(1,1)} (\mathcal{PT})^{-1} = H_k^{(1,1)} \quad (S34)$$

where  $\mathbb{F}_2$  and  $\mathbb{F}_4$  are the two imaginary Dirac matrices. Since  $(\mathcal{PT})^2 = -\mathbb{1}_4$ , it follows that matrices  $H_k^{(1,1)}$  belong to the symplectic class [26], which corresponds to nodal class AII of Ref. [27]. Energy bands in this symmetry class exhibit two-fold Kramers degeneracies in the spectrum, while robust band degeneracies occurring at generic  $\mathbf{k}$ -points are of codimension  $\mathfrak{d} = 5$  [26, 27] and therefore do not occur inside the 4D  $BZ^{(1,1)}$ .

On the other hand, robust point nodes may generically occur inside the five-dimensional space spanned by  $(\mathbf{k}, m)$ . Indeed, as manifested by the phase diagram in Fig. 1(b), topological phase transitions at  $m \in \{0, \pm 2, \pm 4\}$  are facilitated through gap closings, which are pinned by inversion symmetry  $\mathcal{P} = \mathbb{F}_5$  to high-symmetry momenta with components  $\{k_j\}_{j=1}^4 \in \{0, \pi\}$ :

$$\mathcal{P} H_k^{(1,1)} \mathcal{P}^{-1} = H_{-\mathbf{k}}^{(1,1)}. \quad (S35)$$

Since Dirac matrices  $\mathbb{F}_5$  have eigenvalues  $\pm 1$ , each with multiplicity two, it follows from the  $m_k \mathbb{F}_5$  term in the Hamiltonian (3)

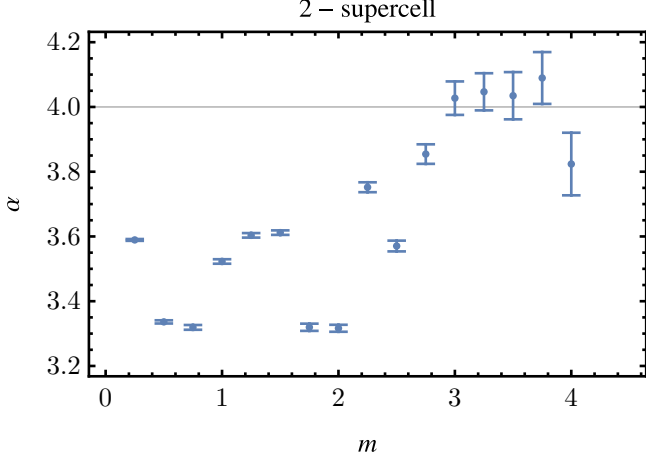


FIG. S6. Low-energy scaling exponent  $\alpha$  as function of the mass parameter  $m$  computed from fitting the 2-supercell density of states with the model  $\rho(E \rightarrow 0) \propto E^\alpha$ . The error bars indicate the standard errors for the estimate of  $\alpha$  (see Section III D for details of the fitting procedure). The horizontal gray line indicates the scaling of  $\alpha = 4$  predicted by the theoretical argument discussed in Section III C 3). Data at  $m = 0$  ( $\alpha = 0.976 \pm 0.002$ ) and  $m > 4$  ( $\alpha = 30 \pm 1$ ) are outside the range shown here, see Fig. S8.

that the consecutive topological phase transitions are driven by inversion of bands of opposite  $\mathcal{P}$ -eigenvalues at the various high-symmetry  $\mathbf{k}$ -points.

Let us remark that when representing the action of  $\mathcal{P}$  on the hyperbolic lattice in the coordinate space, we encounter certain non-uniqueness; namely, there are several distinct points of inversion center that are not related by symmetry of the  $\{8, 8\}$  lattice. These inversion points respectively correspond to: vertices/sites (black dots in Fig. S3), mid-points of edges (green triangle in Fig. S3), and centers of faces (orange squares in Fig. S3) of the  $\{8, 8\}$  lattice. Nevertheless, the inversion operations with respect to these distinct points belong to the same conjugacy class in the hyperbolic point group  $G^{(1)} := \Delta^+/\Gamma^{(1)}$ , where  $\Delta^+ = \Delta^+(2, 8, 8)$  is the triangle group of the  $\{8, 8\}$  lattice [5, 19] and  $\Gamma^{(1)}$  is the translation group associated with the primitive unit cell. It follows that all the specified inversion centers transform the hyperbolic momentum in the same way,  $\mathcal{P} : \mathbf{k} \mapsto -\mathbf{k}$ , and each can, therefore, be interpreted as the coordinate-space equivalent of the inversion symmetry in Eq. (S35).

We next analyze how the notions of  $\mathcal{P}$  and  $\mathcal{T}$  symmetry, and of their composition  $\mathcal{PT}$ , generalize to the 6D BZ $^{(2,1)}$  associated with the hyperbolic Bloch Hamiltonian  $H_{\mathbf{k}}^{(2,1)}$  on the 2-supercell, specified in Eqs. (S25–S26). Let us remind that a hyperbolic crystalline symmetry  $g$  transforms momentum components inside the 6D BZ $^{(2,1)}$  by a linear transformation  $\mathbf{k} \mapsto \mathbf{k}' = M_g \cdot \mathbf{k}$ , where we call  $M_g \in \text{GL}(6, \mathbb{Z})$  the point-group matrix of  $g$  [7]. If  $g$  is a symmetry of the studied model, then the hyperbolic Bloch Hamiltonians  $H_{\mathbf{k}}^{(2,1)}$  and  $H_{\mathbf{k}'}^{(2,1)}$  are related by a linear (unitary or antiunitary) transformation, and consequently the energy spectra at  $\mathbf{k}$  and  $\mathbf{k}'$  are identical.

We first analyze the effect of time-reversal symmetry. Since

$\mathcal{T}$  does not act on spatial coordinates, it does not induce a non-trivial permutation of the boundaries of the 2-supercell. However, being an antiunitary operator,  $\mathcal{T}$  acts by complex conjugation on the twisted boundary conditions across the 2-supercell edges. The conjugation results in flipping the sign of all momentum components, implying  $M_{\mathcal{T}} = -\mathbb{1}_6$ , and there exists a unitary matrix  $U_{\mathcal{T}}$  such that

$$H_{M_{\mathcal{T}} \cdot \mathbf{k}}^{(2,1)} = U_{\mathcal{T}} \cdot [H_{\mathbf{k}}^{(2,1)}]^* \cdot U_{\mathcal{T}}^\dagger \quad (\text{S36})$$

with the specific form of  $U_{\mathcal{T}} = \sigma_0 \otimes (\mathbb{F}_1 \mathbb{F}_3) \mathcal{K}$ .

In contrast to the primitive cell, the discussion of inversion symmetry for the 2-supercell branches into two cases; this is because the various choices of the inversion center now fall into *two* conjugacy classes in the (enlarged) point group  $G^{(2)} := \Delta/\Gamma^{(2)}$ , where  $\Gamma^{(2)}$  is the (reduced) translation group of the 2-supercell. Specifically, the inversion  $\mathcal{P}^V$  with respect to vertices/sites (black dots in Fig. S3) and inversion  $\mathcal{P}^F$  with respect to centers of faces (orange square in Fig. S3) of the  $\{8, 8\}$  lattice are *distinguished* from the inversion  $\mathcal{P}^E$  with respect to the mid-points of edges (green triangle in Fig. S3) of the  $\{8, 8\}$  lattice. For this reason, to understand the full implications of inversion symmetry on the spectrum of  $H_{\mathbf{k}}^{(2,1)}$ , one has to analyze the constraints imposed by both  $\mathcal{P}^{V,F}$  and  $\mathcal{P}^E$ .

We begin by considering the inversion  $\mathcal{P}^V$  with respect to a vertex (which is equivalent to considering  $\mathcal{P}^F$ ). By specifically taking the vertex in the center of the primitive cell, we recognize from the arrangement in Fig. S3 that  $\mathcal{P}^V$  permutes the subscripts of the translation generators as follows:

$$(1, 2, 3, 4, 5, 6, \alpha, \beta) \mapsto (5, 6, \alpha, \beta, 1, 2, 3, 4). \quad (\text{S37})$$

For 1D IRs, the relators among the eight generators of  $\Gamma^{(2)}$  imply that  $k_\alpha = -k_1 - k_3 - k_5$  and  $k_\beta = -k_2 - k_4 - k_6$  [19], i.e., they are uniquely specified by the other six momentum components. Therefore,  $\mathcal{P}^V$  transforms momentum components as  $\mathbf{k} \mapsto M_{\mathcal{P}^V} \cdot \mathbf{k}$  with

$$M_{\mathcal{P}^V} = \begin{pmatrix} 0 & 0 & 0 & 0 & 1 & 0 \\ 0 & 0 & 0 & 0 & 0 & 1 \\ -1 & 0 & -1 & 0 & -1 & 0 \\ 0 & -1 & 0 & -1 & 0 & -1 \\ 1 & 0 & 0 & 0 & 0 & 0 \\ 0 & 1 & 0 & 0 & 0 & 0 \end{pmatrix}. \quad (\text{S38})$$

We find that  $\mathcal{P}^V$  constraints the hyperbolic Bloch Hamiltonian for 2-supercell as

$$H_{M_{\mathcal{P}^V} \cdot \mathbf{k}}^{(2,1)} = U_{\mathcal{P}^V, \mathbf{k}} \cdot H_{\mathbf{k}}^{(2,1)} \cdot U_{\mathcal{P}^V, \mathbf{k}}^\dagger, \quad (\text{S39})$$

where

$$U_{\mathcal{P}^V, \mathbf{k}} = \begin{pmatrix} 1 & 0 \\ 0 & e^{-i(k_2+k_3+k_4+k_5)} \end{pmatrix} \otimes \mathbb{F}_5. \quad (\text{S40})$$

We further identify  $\mathcal{P}^V$ -invariant momenta by solving for  $\mathbf{k} \stackrel{!}{=} M_{\mathcal{P}^V} \cdot \mathbf{k}$  (mod  $2\pi$  in each of the six components), which defines four two-dimensional planes

$$\begin{aligned} \mathcal{M}_{s_1, s_2} = \{ & (k_1, k_2, -k_1 + s_1, -k_2 + s_2, k_1, k_2) | \dots \\ & \dots | k_{1,2} \in [-\pi, +\pi]\} \subset \text{BZ}^{(2,1)} \end{aligned} \quad (\text{S41})$$

where  $s_{1,2} \in \{0, \pi\}$ . Within these planes, the exponential in Eq. (S40) evaluates to

$$e^{-i(k_2+k_3+k_4+k_5)}|_{\mathcal{M}_{s_1,s_2}} = e^{-i(s_1+s_2)} \in \{\pm 1\}, \quad (\text{S42})$$

and the eigenvalues of  $U_{\mathcal{P}\mathcal{V}}$  within the high-symmetry planes are  $\pm 1$ , each with multiplicity four.

If inversion of bands with opposite  $\mathcal{P}^V$  eigenvalue occurs inside  $\mathcal{M}_{s_1,s_2}$ , then these bands are prevented from hybridization and a  $\mathcal{P}^V$ -protected nodal line is formed inside the plane  $\mathcal{M}_{s_1,s_2}$ . Crucially, as  $|m|$  decreases across the critical value  $|m_c| = 4$ , band inversion occurs inside the 4D BZ of  $H_k^{(1,1)}$  at  $\mathbf{k}^{(4D)} = (0, 0, 0, 0)$  (for  $m_c = -4$ ) resp. at  $\mathbf{k}^{(4D)} = (\pi, \pi, \pi, \pi)$  (for  $m_c = +4$ ). Owing to the zone-folding of immersion  $\iota$  in Eq. (S23), both four-momenta are mapped to the same six-momentum  $\mathbf{k} = 0$  inside the plane  $\mathcal{M}_{0,0}$ . Therefore, we conclude that the topological transitions at  $|m_c| = 4$  are associated with the formation of a nodal line inside the plane  $\mathcal{M}_{0,0}$ . This prediction, rooted in symmetry analysis, agrees with the analytical calculation presented in Appendix III C 1.

Next, we consider implications of the inversion  $\mathcal{P}^E$  with respect to the mid-point of an edge of the  $\{8, 8\}$  lattice (green triangle in Fig. S3). To understand how  $\mathcal{P}^E$  acts on the momenta inside  $\text{BZ}^{(2,1)}$ , we use GAP [8, 9] to express conjugations  $\mathcal{P}^E \tilde{\gamma}_j (\mathcal{P}^E)^{-1}$  of the generators  $\{\tilde{\gamma}_j\}_{j=1}^6$  of the translation group  $\Gamma^{(2)}$  as composite words in  $\{\tilde{\gamma}_j\}_{j=1}^6$  [7]. We obtain

$$\tilde{\gamma}_1 \mapsto \tilde{\gamma}_1^{-1}, \quad (\text{S43a})$$

$$\tilde{\gamma}_2 \mapsto \tilde{\gamma}_2^{-1}, \quad (\text{S43b})$$

$$\tilde{\gamma}_3 \mapsto \tilde{\gamma}_2 \tilde{\gamma}_3^{-1} \tilde{\gamma}_2^{-1}, \quad (\text{S43c})$$

$$\tilde{\gamma}_4 \mapsto \tilde{\gamma}_2 \tilde{\gamma}_3 \tilde{\gamma}_4^{-1} \tilde{\gamma}_3^{-1} \tilde{\gamma}_2^{-1}, \quad (\text{S43d})$$

$$\tilde{\gamma}_5 \mapsto \tilde{\gamma}_2 \tilde{\gamma}_3 \tilde{\gamma}_4 \tilde{\gamma}_5^{-1} \tilde{\gamma}_4^{-1} \tilde{\gamma}_3^{-1} \tilde{\gamma}_2^{-1}, \quad (\text{S43e})$$

$$\tilde{\gamma}_6 \mapsto \tilde{\gamma}_2 \tilde{\gamma}_3 \tilde{\gamma}_4 \tilde{\gamma}_5^{-1} \tilde{\gamma}_1^{-1} \tilde{\gamma}_6^{-1} \tilde{\gamma}_4^{-1} \tilde{\gamma}_2^{-1} \tilde{\gamma}_1, \quad (\text{S43f})$$

which at the level of Abelian representations  $\rho(\tilde{\gamma}_j) = e^{ik_j}$  simplifies to a diagonal point-group matrix  $M_{\mathcal{P}^E} = -\mathbb{1}_6$ . Since  $\mathcal{P}^E$  exchanges the two sites within the 2-supercell, we find that

$$H_{M_{\mathcal{P}^E} \cdot \mathbf{k}}^{(2,1)} = U_{\mathcal{P}^E} \cdot H_{\mathbf{k}}^{(2,1)} \cdot U_{\mathcal{P}^E}^\dagger, \quad (\text{S44})$$

where

$$U_{\mathcal{P}^E} = \sigma_1 \otimes \mathbb{F}_5. \quad (\text{S45})$$

Importantly, note that the composition  $\mathcal{P}^E \mathcal{T}$  acts trivially on  $\text{BZ}^{(2,1)}$ :

$$M_{\mathcal{P}^E \mathcal{T}} = M_{\mathcal{P}^E} \cdot M_{\mathcal{T}} = \mathbb{1}_6, \quad (\text{S46})$$

while inside the Hilbert space of Bloch states at  $\mathbf{k}$  it acts by an antiunitary transformation:

$$U_{\mathcal{P}^E \mathcal{T}} = U_{\mathcal{P}^E} \cdot U_{\mathcal{T}} = \sigma_1 \otimes (\mathbb{F}_1 \mathbb{F}_3) \mathcal{K}. \quad (\text{S47})$$

Since  $(U_{\mathcal{P}^E \mathcal{T}})^2 = -\mathbb{1}_6$ , we conclude that Hamiltonian matrices  $H_{\mathbf{k}}^{(2,1)}$  belong to the symplectic class (nodal class AII of Ref. [27]) whose spectrum exhibits Kramers degeneracy and

the band nodes are generically of codimension  $\mathfrak{d} = 5$ . This is consistent with the observed formation of  $(6 - 5) = 1$ -dimensional nodal lines inside  $\text{BZ}^{(2,1)}$ , as illustrated with numerically extracted data in Fig. S4.

As discussed in the *Nodal ring* section of the main text, if one assumes a linear dispersion of the energy bands near the band node in all directions perpendicular to the node, then the expected DOS scaling is  $\rho(E) \propto E^{\mathfrak{d}-1}$ , i.e., we anticipate  $\rho(E) \propto E^4$  for the hyperbolic non-Abelian semimetal. While this theoretical prediction appropriately describes the scaling of numerically obtained DOS data for  $m \in (3, 4)$ , where the 2-supercell description identifies a single nodal ring, we observe in Fig. S6 a noticeable deviation to somewhat lower values of the DOS exponent for  $m \in (0, 3)$ , where the nodal manifold acquires a complicated structure. This observation suggests that the assumption on linear band dispersion fails in some directions near some locations on the nodal manifold: either for symmetry reasons (e.g. nodal line located along a high-symmetry line, where symmetry forbids linear terms), or due to intersections of multiple nodal rings (i.e., nodal chain), or accidentally (which may be expected due to the large extent of the nodal manifold).

We finally tackle the particular case of  $m = 0$ , where Fig. S4 suggests a higher-dimensional nodal manifold, and Fig. S6 indicates an altered scaling of the density of states. For this choice of the mass parameter, an additional sublattice symmetry  $\mathcal{S}$  arises, which leaves the six-dimensional momentum  $\mathbf{k}$  invariant ( $M_{\mathcal{S}} = \mathbb{1}_6$ ). It acts on the Hilbert space by a unitary matrix:

$$U_{\mathcal{S}} = \sigma_3 \otimes \mathbb{1}_4, \quad (\text{S48})$$

and that flips the sign of energy:

$$U_{\mathcal{S}} \cdot H_{\mathbf{k}}^{(2,1)} \cdot U_{\mathcal{S}}^{-1} = -H_{\mathbf{k}}^{(2,1)}. \quad (\text{S49})$$

Since  $\mathcal{S}$  anticommutes with  $\mathcal{P}^E \mathcal{T}$  (i.e., the “sublattice parity is odd” per the terminology of Ref. [27]), the Hamiltonian  $H_{\mathbf{k}}^{(2,1)}$  belongs to nodal class DIII at  $m = 0$ . The sublattice symmetry thereby reduces the codimension for node formation to  $\mathfrak{d} = 2$  [27], which implies that the nodal manifold becomes four-dimensional in  $\text{BZ}^{(2,1)}$  (so that it completely fills the three-dimensional projection in the  $m = 0$  panel of Fig. S4). Assuming again the linear dispersion in the two directions perpendicular to the nodal manifold, the expect DOS scaling is  $\rho(E) = \int d^2 k_\perp \delta(E - v|k_\perp|) \propto E$ . This theoretical prediction is consistent with the observed drop in the numerically extracted exponent visible in Fig. S6.

## D. Density of states for larger $n$ -supercells

### 1. Density of states from random sampling

We systematically study the low-energy DOS as a function of supercell size  $n$  and mass parameter  $m$  to gain some understanding of the possible phase diagrams arising from the inclusion of higher-dimensional irreducible representations

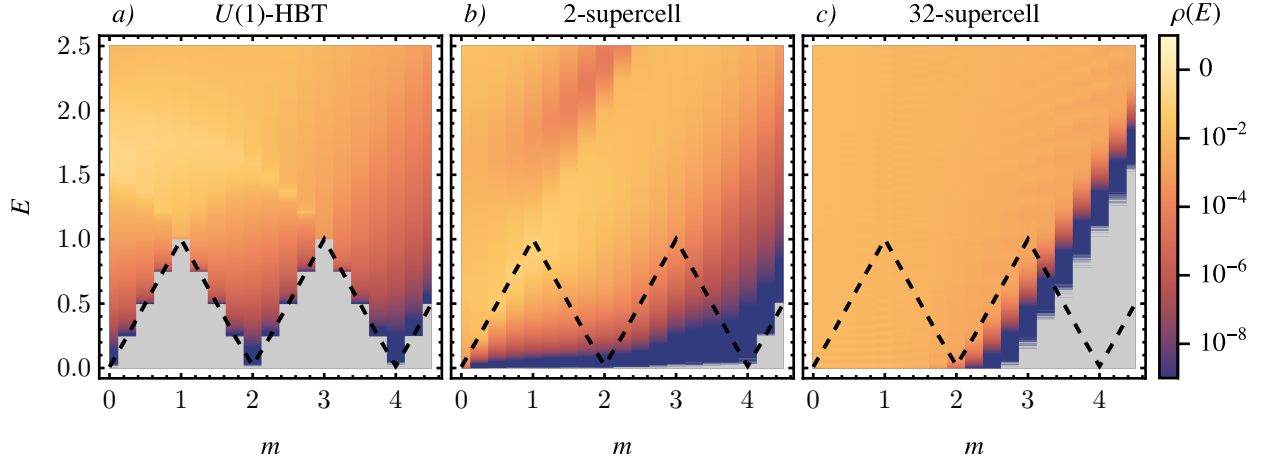


FIG. S7. Density of Abelian states  $\rho(E; m)$  obtained from (a) the primitive cell, corresponding to U(1) hyperbolic band theory (HBT), (b) the 2-supercell, and (c) the 32-supercell as a function of energy  $0 \leq E \leq 2.5$  and mass parameter  $0 \leq m \leq 4.5$  from random sampling with (a,c)  $10^9$  and (b)  $10^{10}$  Abelian momenta. The density is shown on a logarithmic scale (legend on the right) Zero values, indicating a true gap in the spectrum for that particular (super-)cell, are shown in gray. The black dashed line indicates the exact gap in the density of U(1) states.

and thus at larger system sizes. To that end, for each of the  $n$ -supercells defined in Eq. (S21), we randomly sampled  $10^9$  ( $10^{10}$  for  $n = 2$ )  $k$ -points in their  $(2n+2)$ -dimensional  $BZ^{(n,1)}$  of U(1) representations, resulting in  $N = 4n \times 10^9$  ( $8 \times 10^{10}$  for  $n = 2$ ) eigenenergies. We then count the collected eigenenergies, producing a histogram of counts  $N_i$  associated with bins of width  $\Delta E = 0.001$  centered at energies in the range  $E_i \in [-8.0005, 8.0005]$ .

Ignoring potential correlations from states at the same Abelian momentum, we assume that the  $N$  states characterized by energy  $E$  are independent samples from the probability distribution  $\rho(E)$ , which is precisely the density of states. Thus, the probability of finding a randomly sampled state in the bin centered at  $E_i$  is

$$p_i = \int_{E_i - \Delta E/2}^{E_i + \Delta E/2} dE \rho(E) \approx \rho(E_i) \Delta E. \quad (\text{S50})$$

The probability of observing  $N_i$  states in the bin centered at  $E_i$  when sampling  $N$ , thus, is given by the binomial distribution  $\mathcal{B}(N, p_i)$ :

$$P(N_i) = \binom{N}{N_i} p_i^{N_i} (1 - p_i)^{N - N_i}, \quad (\text{S51})$$

with mean  $Np_i = N\rho(E_i)\Delta E$  and variance  $\sigma^2(N_i) = Np_i(1 - p_i)$ . This allows us to estimate  $p_i$  via the estimator  $\hat{p}_i = N_i/N$  and thus  $y_i = p_i/\Delta E \approx \rho(E_i)$  via the estimator

$$\hat{y}_i = \frac{\hat{p}_i}{\Delta E} = \frac{N_i}{N\Delta E}. \quad (\text{S52})$$

The associated standard deviation is

$$\begin{aligned} \sigma(y_i) &= \frac{\sigma(N_i)}{N\Delta E} = \frac{\sqrt{Np_i(1 - p_i)}}{N\Delta E} \\ &= \sqrt{\frac{y_i(1/\Delta E - y_i)}{N}}, \end{aligned} \quad (\text{S53})$$

which can be estimated by

$$\hat{\sigma}(y_i) = \sqrt{\frac{\hat{y}_i(1/\Delta E - \hat{y}_i)}{N}}. \quad (\text{S54})$$

The resulting data  $\hat{y}_i$  representing  $\rho(E)$  is shown in Fig. S7 in the energy range  $0 \leq E \leq 2.5$  as a function of the mass parameter  $0 \leq m \leq 4.5$  for (a) U(1)-HBT, (b) the 2-supercell, and (c) the 32-supercell.

For U(1)-HBT [Fig. S7(a)] we find perfect agreement with the expected semimetallic gap closing at  $m = 0, 2, 4$  and with insulators at the intermediate mass parameters with maximal gaps at  $m = 1, 3$ . Figure S7(b) shows that there are non-Abelian in-gap states across the full range  $0 < m < 4$  with a semimetallic (i.e., power-law-scaling) density of states. In addition, we observe a quantitative depletion of DOS in the immediate neighborhood of  $E = 0$  with increasing  $m > 2$  (which could be attributable to shrinking of the nodal manifold, cf. Fig. S4) and a gap opening after  $m = 4$  (which corresponds to disappearance of the nodal-line ring), with a band edge that follows the Abelian band edge for  $m > 4$ . Note that despite the quantitative depletion, we have seen in Fig. S6 that the scaling of the DOS with  $E$  remains approximately constant, with exponent  $\alpha \in (3.3, 4.1)$ .

Going to larger supercells and finally to the 32 supercell, for which the data is shown in Fig. S7(c), we observe a qualitatively different behavior at different values of the mass parameter  $m$ . First, in the range  $0 < m \lesssim 2$ , the Abelian gap is clearly filled up with more and more non-Abelian states seemingly converging towards a metallic DOS in the thermodynamic limit. On the other hand, the region  $3 \lesssim m \leq 4$  is depleted of further states (as is the trivially insulating region  $m > 4$ ), such that we expect an insulator in the thermodynamic limit. The transition between the two phases most probably lies in the range  $2 < m < 3$ . More detailed discussion of our findings appears in Section III D.

Before concluding, two remarks are in order. First, the non-Abelian states arising from finite-dimensional irreducible representations, in particular those shown in Fig. S7(b), are still present in the thermodynamic limit, even if they occur with a vanishingly small weight. Second, the density of Abelian states of any of the studied supercells ( $2 \leq n \leq 32$ ) in the range  $0 \leq m \leq 4$  is, strictly speaking, always *semimetallic* with

- (i) a narrow dip at  $E = 0$  due to inherent numerical artifacts of the supercell technique (see Sec. II.A.3 of Supplemental Material to Ref. 19) in the metallic regime, and
- (ii) with heavily suppressed tails in the insulating regime.

Therefore, special care is necessary to distinguish insulating resp. metallic spectra from truly semimetallic ones.

## 2. Fitting the low-energy density of states

For a more quantitative characterization of the DOS arising from the different supercells, we repeat the fitting procedure applied in the earlier Section III C 2 to the 2-supercell, assuming the model  $\rho(E \rightarrow 0) \propto E^\alpha$ . Because we are not directly fitting the DOS  $\rho(E)$  but a *histogram*, i.e.,  $\rho(E)$  integrated over disjoint energy ranges, we have to be careful in the range  $0 < m \lesssim 3$ , where the finite bin-width might have smeared out the anticipated DOS dip [cf. the remark (i) above], such that the histogram nevertheless indicates a finite  $\rho(E = 0)$ . To account for these subtleties, we apply a multistep fitting strategy as outline below.

In the first step, we determine whether the DOS *data* (for the given bin width) is metallic or semimetallic. To that end, we consider the *cumulative* density of states (with positive energy),

$$F_\rho(E) = \int_0^E dE' \rho(E'), \quad (\text{S55})$$

which can be obtained from the observed histogram as follows (assuming  $i = 0$  corresponds to the bin centered at  $E = 0$ ):

$$z_i = F_\rho(E_i + \Delta E/2) = \Delta E \left( \frac{y_0}{2} + \sum_{0 < j \leq i} y_j \right), \quad (\text{S56})$$

where we made use of the spectral symmetry  $\rho(-E) = \rho(E)$  to split the bin at zero energy. Going to the cumulative density of states has two main advantages: First, it averages over the oscillations that are typically observed in the Abelian DOS of finite supercells [19] and second, it removes the bias of the binning, since the  $z_i$  are actually evaluations of  $F_\rho$  at certain energies, unlike  $y_i$  which only correspond to  $\rho(E_i)$  in the limit  $\Delta E \rightarrow 0$ .

Next, we perform a linear least-square fit of the cumulative density of states as a function of energy in a log-log-scale, i.e., we set up the following linear model

$$\log(z_i) = (\alpha + 1) \log(E_i + \Delta E/2) + \beta \quad (\text{S57})$$

obtained from integrating the model  $\rho(E \rightarrow 0) \propto E^\alpha$ . We constrain the fit to a very small energy window [ $E_{\min}, E_{\max}$ ]

near  $E = 0$  chosen such that  $F_\rho(E_{\min}) \geq 10^{-9}$  and  $E_{\max} = E_{\min} + 15\Delta E$ . A linearly increasing cumulative DOS indicates a metallic behavior,  $\alpha = 0$ , allowing us to detect those cases; here we set a threshold  $\alpha < 0.5$ . For the cases that are deemed to be metallic, the extracted values  $\alpha$  are shown in Fig. S8 as orange data points. Note that parameter errors obtained from the least-square fit have to be interpreted with care. Since the fitting is done in a log-log-scale and furthermore even the errors in the original data are not normally distributed (which we partially take into account for the second step as discussed below), the statistical assumptions that would allow us to interpret the parameter errors as confidence intervals are not satisfied. Nevertheless, the errors do give a rough (relative) idea of how close the scaling is to zero and therefore we include error bars for the orange data points in Fig. S8.

In the second step of the procedure, we perform a non-linear least-square fit of the DOS data  $\hat{y}_i$ . Both the model and the energy window  $[E_{\min}, E_{\max}]$  depend on the previous estimate of  $\alpha$ . The lower bound of the energy window is now determined by the condition  $\rho(E \geq E_{\min}) > 5 \times 10^{-8}$ , while the width  $E_{\max} - E_{\min}$  is  $15\Delta E$  for  $\alpha \leq 1.2$  (with the exception of  $m = 0$ , where it is always  $10\Delta$ ) and  $100\Delta E$  for  $\alpha > 1.2$ . The motivation for these different choices of the fitting range is the significantly larger deviation from a power law behavior in the metallic regime  $m \lesssim 3$  due to subleading corrections. In particular, we explicitly include subleading corrections to the constant term in the fit model for the metallic regime, cf. Eq. (S59), despite the significantly smaller energy range.

To compensate for the variation of the variance of  $y_i$  with  $i$ , a weighted fitting procedure is used with weights proportional to the inverse of the standard deviation:

$$w_i \propto \frac{1}{\hat{\sigma}(y_i)} \approx \sqrt{\frac{N\Delta E}{\hat{y}_i}} \propto \frac{1}{\sqrt{\hat{y}_i}}, \quad (\text{S58})$$

where we used Eq. (S54) and that typically  $\hat{y}\Delta E \ll 1$ . Note that this does not compensate for the non-normality of the binomial distribution according to which the  $y_i$  are distributed. While the binomial distribution can be approximated by a normal distribution with same mean and variance for large  $N$ , such an approximation is typically not very good if  $p_i$  is close to 0 or 1. Thus, while the parameter errors are not unreasonable, they have to be interpreted with care.

The non-linear models used in the fitting are as follows. In the metallic regime, we assume

$$\hat{y}_i = \rho_0 + \rho_1 E^{\alpha_1}, \quad (\text{S59})$$

while in the semimetallic/insulating regime, we assume

$$\hat{y}_i = \rho_1 E^{\alpha}. \quad (\text{S60})$$

Note that  $\alpha_1$  is *not* the leading order scaling but we force a term  $\rho_0$  due to our previous estimate of  $\alpha$  resulting in a value close to zero, see orange data points in Fig. S8. Thus, we obtain estimates of  $\alpha$  for the semimetallic/insulating regime as well; these are shown as blue data points in Fig. S8. Finally, in the metallic regime  $0 < m < 3$ , we extract estimates of  $\rho_0$ , corresponding to  $\rho(E = 0)$ , which are shown in Fig. S9. These can be interpreted as a measure of the ‘Fermi surface extent’.

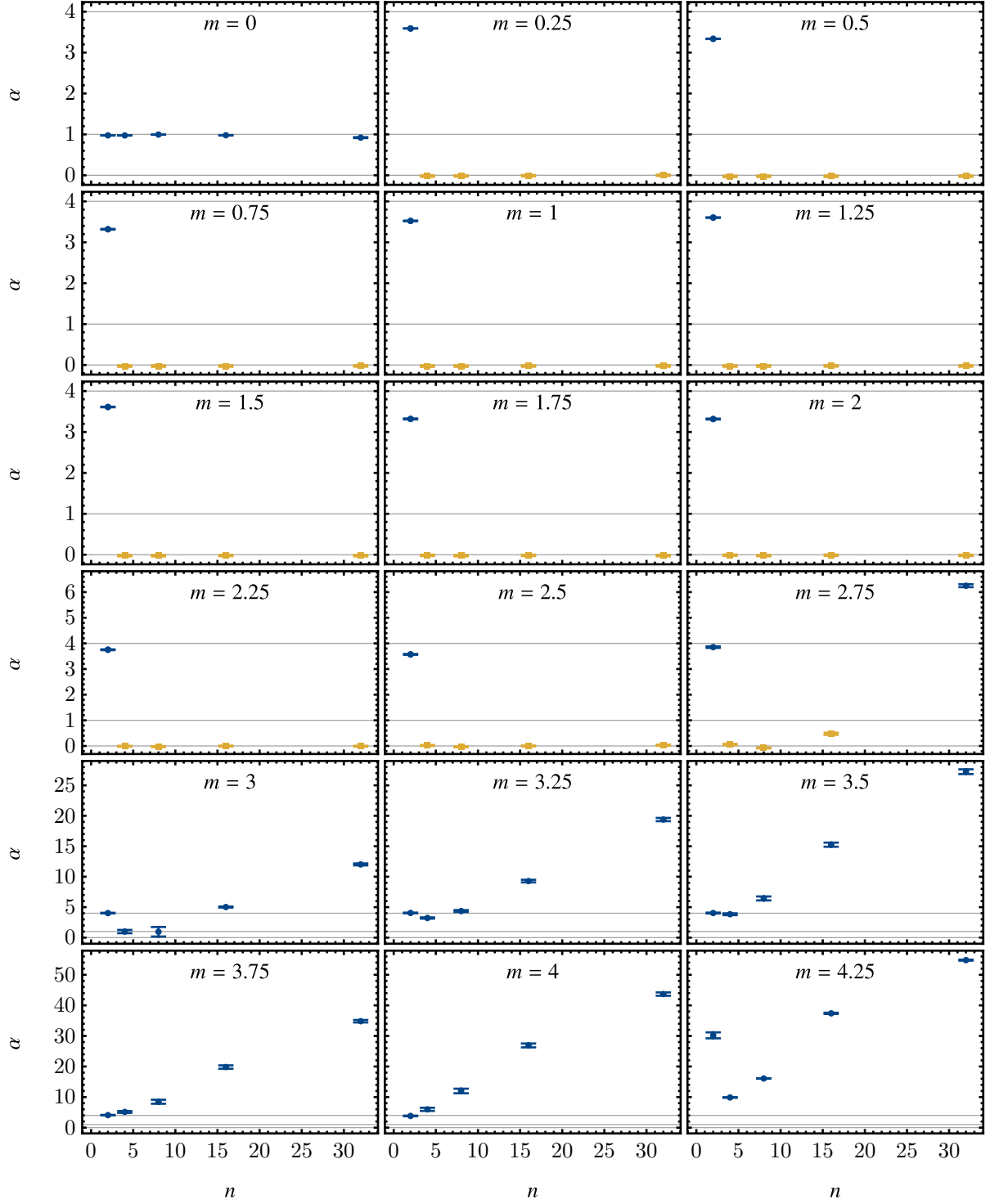


FIG. S8. Low-energy scaling exponent  $\alpha$  as function of supercell size  $n$  for different values of the mass parameter  $m$ , obtained using the fitting procedure described in Section III D 2. The blue data points have been obtained from a weighted non-linear least-square fit of the  $n$ -supercell density of states with model  $\rho(E \rightarrow 0) \propto E^\alpha$  and the error bars indicate the standard errors but should be interpreted with care. The orange data points have been obtained from a linear least-square fit of the cumulative density of states with model  $\rho(E \rightarrow 0) \propto E^{\alpha+1}$  on a log-log-scale. The horizontal gray lines indicates the following values: 0, 1, and 4.

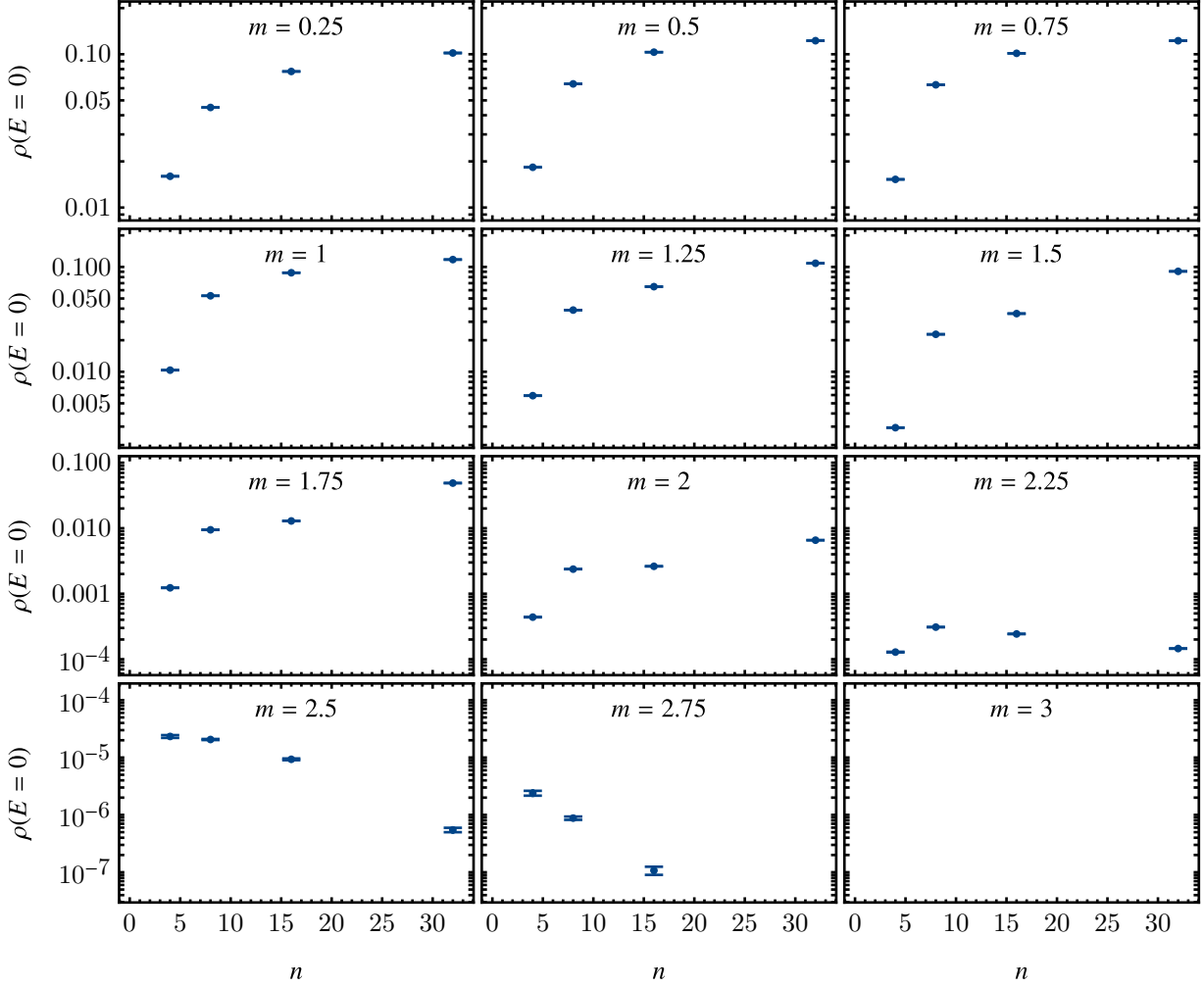


FIG. S9. Density of states at zero energy  $\rho(E = 0)$  as function of supercell size  $n$  for different values of the mass parameter  $m$ . The data have been obtained from a weighted non-linear least-square fit of the  $n$ -supercell density of states with model  $\rho(E \rightarrow 0) = \rho_0 + \rho_1 E^{\alpha_1}$  and the error bars indicate the standard errors but should be interpreted with care. Note that only data for  $(n, m)$  with a metallic density of states are shown. In particular,  $n = 32$  for  $m = 2.75$  and any  $n$  for  $m = 3$  are semimetallic such that no data points are shown.

### 3. Metal-to-insulator transition for large $n$ -supercells

Let us finally discuss how the trends observed in Fig. S7(c) and described in Sec. III D 1 are correlated with the in-depth analysis of the DOS scaling shown in Figs. S8 and S9.

For  $0 < m \lesssim 2$  our fitting procedure indicates a metallic DOS (yellow data in Fig. S8) for all supercells with  $n > 2$ , with  $\rho(E = 0)$  (Fig. S9) that monotonously grows with the supercell size  $n$ . Therefore, we anticipate the model to be in the metallic phase in the thermodynamic limit for this range of the mass parameter. Furthermore, observe that  $\rho(E = 0)$  for the 32-supercell peaks for  $m \in (0.5, 0.75)$ , and shrinks to a smaller value at  $m = 0.25$ . This could be interpreted as a shrinking of the Fermi surface extent, vanishing altogether at  $m = 0$  where the DOS appears semimetallic for all studied  $n$ -supercells.

The points  $2 < m \lesssim 3$  appear to be close to the metal-to-insulator transition. Specifically, for  $m = 2.25$  the zero-energy DOS  $\rho(E = 0)$  seems to converge to a small value below  $2 \times 10^{-4}$  (potentially to zero). For  $m = 2.5$ , although the

fits for all supercells with  $n > 2$  appear metallic in Fig. S8, a look at Fig. S9 indicates a rapidly shrinking  $\rho(E = 0)$ . Therefore, we expect that the point  $m = 2.5$  is already on the insulating side of the phase boundary. For  $m = 2.75$ , the DOS appears metallic for the intermediate values of the supercell size  $n \in \{4, 8, 16\}$ , but ultimately becomes semimetallic with large  $\alpha \approx 6.3$  for the 32-supercell, suggesting an insulating phase in the thermodynamic limit.

The proximity to the critical point still leaves a mark on the extracted  $\alpha(n)$  for  $m = 3$ . Namely, while the 2-supercell suggests semimetallic  $\alpha \approx 4$ , the 4-supercell and the 8-supercell are characterized by a significantly smaller DOS scaling exponent  $\alpha \approx 1$ , reminiscent of the onset of the metallic phase at lower values of  $m$ . This trend at intermediate values of  $n$  is overturned for supercells with  $n \in \{16, 32\}$ . A similar but much less pronounced dip in  $\alpha$  is also observed for the 4-supercell at  $m = 3.25$ . Finally, for  $m \gtrsim 3.25$ , the fitted scaling exponent  $\alpha$  grows dramatically with  $n$ , providing a clear sign of an insulating phase in the thermodynamic limit.

- 
- [1] F. Sausset and G. Tarjus, Periodic boundary conditions on the pseudosphere, *J. Phys. A: Math. Theor.* **40**, 12873 (2007).
- [2] J. Maciejko and S. Rayan, Automorphic Bloch theorems for hyperbolic lattices, *Proc. Natl. Acad. Sci. U.S.A.* **119** (2022).
- [3] F. R. Lux and E. Prodan, Spectral and combinatorial aspects of cayley-crystals, *Annales Henri Poincaré* [10.1007/s00023-023-01373-3](https://doi.org/10.1007/s00023-023-01373-3) (2023).
- [4] F. R. Lux and E. Prodan, Converging Periodic Boundary Conditions and Detection of Topological Gaps on Regular Hyperbolic Tessellations, *Phys. Rev. Lett.* **131**, 176603 (2023).
- [5] I. Boettcher, A. V. Gorshkov, A. J. Kollár, J. Maciejko, S. Rayan, and R. Thomale, Crystallography of hyperbolic lattices, *Phys. Rev. B* **105**, 125118 (2022).
- [6] A. Chen, H. Brand, T. Helbig, T. Hofmann, S. Imhof, A. Fritzsche, T. Kießling, A. Stegmaier, L. K. Upreti, T. Neupert, T. Bzdušek, M. Greiter, R. Thomale, and I. Boettcher, Hyperbolic matter in electrical circuits with tunable complex phases, *Nat. Commun.* **14**, 622 (2023).
- [7] A. Chen, Y. Guan, P. M. Lenggenhager, J. Maciejko, I. Boettcher, and T. Bzdušek, Symmetry and topology of hyperbolic Haldane models, *Phys. Rev. B* **108**, 085114 (2023).
- [8] F. Röber, The GAP package LINS, <https://github.com/FriedrichRöber/LINS> (2020).
- [9] GAP, *GAP – Groups, Algorithms, and Programming, Version 4.11.1*, The GAP Group (2021).
- [10] D. Firth, *An Algorithm to Find Normal Subgroups of a Finitely Presented Group, up to a Given Finite Index*, Ph.D. thesis, University of Warwick (2004).
- [11] D. J. S. Robinson, *A Course in the Theory of Groups*, 2nd ed. (Springer, New York, 1996).
- [12] T. Bzdušek and J. Maciejko, Flat bands and band-touching from real-space topology in hyperbolic lattices, *Phys. Rev. B* **106**, 155146 (2022).
- [13] X.-L. Qi, T. L. Hughes, and S.-C. Zhang, Topological field theory of time-reversal invariant insulators, *Phys. Rev. B* **78**, 195424 (2008).
- [14] M. Mochol-Grzelak, A. Dauphin, A. Celi, and M. Lewenstein, Efficient algorithm to compute the second Chern number in four dimensional systems, *Quantum Sci. Technol.* **4**, 014009 (2018).
- [15] T. Fukui, Y. Hatsugai, and H. Suzuki, Chern numbers in discretized Brillouin zone: efficient method of computing (spin) Hall conductances, *J. Phys. Soc. Japan* **74**, 1674 (2005).
- [16] T. Tummuru, A. Chen, P. M. Lenggenhager, T. Neupert, J. Maciejko, and T. Bzdušek, *Supplementary Data and Code for Hyperbolic non-Abelian semimetal* (2023).
- [17] Á. Nagy and S. Rayan, On the hyperbolic bloch transform, *Annales Henri Poincaré* **25**, 1713–1732 (2023).
- [18] J. B. Bronzan, Parametrization of  $SU(3)$ , *Phys. Rev. D* **38**, 1994 (1988).
- [19] P. M. Lenggenhager, J. Maciejko, and T. Bzdušek, Non-Abelian Hyperbolic Band Theory from Supercells, *Phys. Rev. Lett.* **131**, 226401 (2023).
- [20] R. Mosseri and J. Vidal, Density of states of tight-binding models in the hyperbolic plane, *Phys. Rev. B* **108**, 035154 (2023).
- [21] R. Miranda, *Algebraic Curves and Riemann Surfaces* (American Mathematical Society, Providence, 1995).
- [22] M. Conder, *Quotients of triangle groups acting on surfaces of genus 2 to 101* (2007).
- [23] P. M. Lenggenhager, J. Maciejko, and T. Bzdušek, *HyperBloch: A Mathematica package for hyperbolic tight-binding models and the supercell method*, <https://github.com/patrick-lenggenhager/HyperBloch> (2023).
- [24] S.-C. Zhang and J. Hu, A Four-Dimensional Generalization of the Quantum Hall Effect, *Science* **294**, 823 (2001).
- [25] S. Ryu, A. P. Schnyder, A. Furusaki, and A. W. W. Ludwig, Topological insulators and superconductors: tenfold way and dimensional hierarchy, *New J. Phys.* **12**, 065010 (2010).
- [26] J. von Neumann and E. Wigner, Über das Verhalten von Eigenwerten bei adiabatischen Prozessen, *Phys. Z.* **30**, 465 (1929).
- [27] T. Bzdušek and M. Sigrist, Robust doubly charged nodal lines and nodal surfaces in centrosymmetric systems, *Phys. Rev. B* **96**, 155105 (2017).